Theses and Dissertations

8-2013

Structural Properties of Ferroelectric Lead (zirconium0.5,Titanium0.5)Oxygen3 Nanotube Array and Electronic Structure of Lao delta-doped strontium titanate

Rajendra Prasad Adhikari
University of Arkansas, Fayetteville

Follow this and additional works at: http://scholarworks.uark.edu/etd

Part of the Condensed Matter Physics Commons, and the Nanoscience and Nanotechnology Commons

Recommended Citation

Adhikari, Rajendra Prasad, "Structural Properties of Ferroelectric Lead (zirconium0.5,Titanium0.5)Oxygen3 Nanotube Array and Electronic Structure of Lao delta-doped strontium titanate" (2013). *Theses and Dissertations*. 883.
http://scholarworks.uark.edu/etd/883

Structural Properties of Ferroelectric Pb(Zr$_{0.5}$,Ti$_{0.5}$)O$_3$ Nanotube Array and Electronic
Structure of Lao δ-doped SrTiO$_3$

Structural Properties of Ferroelectric Pb(Zr$_{0.5}$,Ti$_{0.5}$)O$_3$ Nanotube Array and Electronic
Structure of Lao δ-doped SrTiO$_3$

A dissertation submitted in partial fulfillment
of the requirements for the degree of
Doctor of Philosophy in Physics

by

Rajendra P. Adhikari
Tribhuvan University
Master of Science in Physics, 2001
University of Rhode Island
Master of Science in Physics, 2007

August 2013
University of Arkansas

This dissertation is approved for recommendation to the Graduate Council.

_____

Dr. Huaxiang Fu
Dissertation Director

_____   _____

Dr. Laurent Bellaiche   Dr. Gregory Salamo
Committee Member   Committee Member

_____   _____

Dr. Michael Lieber   Dr. Hameed Naseem
Committee Member   Committee Member

Abstract

In this Dissertation we begin with two introductions on: 1) ferroelectricity and related phenomena, and 2) novel properties of Oxide electronics and the generation of two dimensional electron gas. We then give theoretical background of density functional theory (including LDA+U) and pseudopotentials.

The first part of research work is about structural, polarization, and dielectric properties of ferroelectric Lead Zirconate Titanate (PZT) solid solution in the form of a nanotube array, embedded in a matrix medium of different ferroelectric strengths. We use the effective Hamiltonian derived from first-principles and finite-temperature Monte Carlo methods to determine the various properties. We revealed different polarization phases of the system in the absence of an external electric field and explained these properties in microscopic detail.

In the second part, we study the effects of compressive biaxial inplane strains on the electronic and structural properties of Lanthanum Oxide δ-doped Strontium Titanate supercell. We use first-principles density functional calculations within the local density approximation including also on-site Coulomb interaction energy. We approached the problem by comparing the band structures, localization of electronic states, and cation-anion displacements of unstrained and strained systems. We found a critical strain above which there are abrupt changes in conduction band dispersions and cation-anion displacements, indicating that inplane biaxial strain can drastically tune the properties of this system, which may have potential technological applications.

Acknowledgments

Contents

List of Figures

List of Tables

Chapter 1

Introduction

1.1 Ferroelectricity

Ferroelectricity is the phenomenon of spontaneous electric polarization found in certain types of crystallographic materials in zero electric field, which can be switched by the application of an external electric field. Materials that possess ferroelectricity are called ferroelectric materials, and those that retain the polarization but are not necessarily switchable are called pyroelectric materials[1]. One class of the ferroelectric materials is the perovskite oxide crystal of chemical formula ABO_3, where A and B are cation elements and O is oxygen. It consists of a five-atom basis cubic structure. It could also be their mixtures like $A(B_{1-x}C_x)O_3$, where x is the mixing factor. Different choices of A and/or B atoms in the perovskite help to tune the transport, magnetic and other physical properties and some have wide technological use. A schematic drawing of the perovskite crystal of the form ABO_3 is shown in Fig.1.1. In its conventional form we show type A atoms on the cube corners, a type B atom on the center of the cube and oxygen atoms on the center of each face. Another equivalent structure may be formed by swapping the atoms A and B.

The initial discovery of ferroelectricity in Rochelle salts did not attract much interest due to its complex crystal structure and chemical formula. However, when ferroelectricity was discovered in barium titanate ($BaTiO_3$), it quickly generated a widespread attention and became one of the most studied perovskite oxide due to its simple structure[2], which also allows theoretical study of ferroelectric materials. In order to describe the origin of ferroelectricity in perovskite materials a double-well potential model can be adopted. In this model, atoms prefer to move away from their high-symmetry centers. The off-centering of B atom inside the oxygen octahedra causes one of the two equivalent polarizations along

1
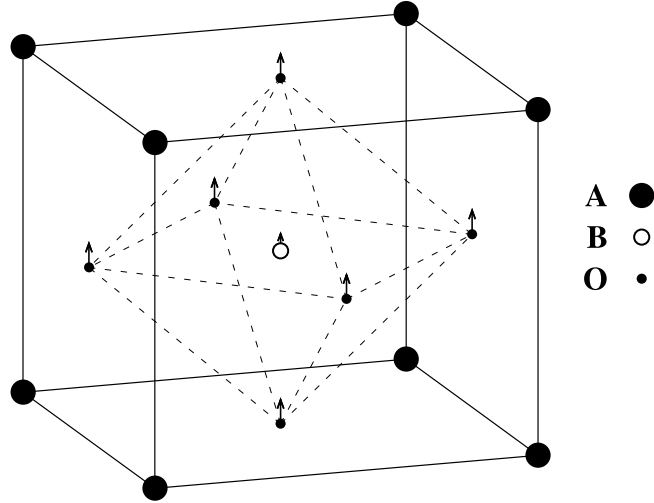
Figure 1.1: Perovskite structure with ABO_3 chemical formula. The dashed lines illustrates the oxygen octahedra that encloses the type B atom.

opposite directions. Fig.1.2 shows the schematic view of this model in which two valleys represent the energy minima for the polar structure and the saddle point at the middle represents the unpolar state in which the B atom is at the center of oxygen octahedra cage.

The delicate balance between long-range Coulomb interactions (favors off-centering) and short-range covalent interactions (favors centro-symmetric structure) determines the ferro-electric nature of the materials[3].

In this study we worked on the ferroelectric Lead Zirconate Titanate $Pb(Zr_{0.5}Ti_{0.5})O_3$ (PZT) and incipient ferroelectric(no ferroelectric phase transition even to 0K) $SrTiO_3$ (STO). In the following sections we discuss a few properties and applications of ferroelectric materials in some detail.
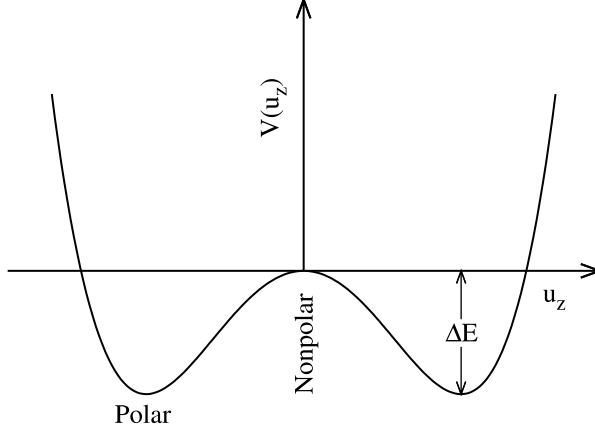
Figure 1.2: Double-well model of ferroelectric polarization. The horizontal axis represents the magnitude of B atom off-centering along z-axis and vertical axis represents the potential energy.

1.2   Phase transition

The phase transition in ferroelectric material is marked by the transition of high symmetry non-polar phases generally known as prototype phases into low symmetry polar phases such as tetragonal or rhombohedral, developing the spontaneous polarization below a certain temperature called the Curie temperature T_c. The phase transition sequence of $BaTiO_3$ (BTO) from higher temperature to lower temperature is cubic to tetragonal [001], tetragonal to orthorhombic [011], and orthorhombic to rhombohedral [111] at temperature 403K, 278K, and 183K, respectively. The phase transition in $PbTiO_3$ (PTO) has only cubic to tetragonal at temperature of 766K, and STO does not have ferroelectric phase transition all the way down to 0K (incipient ferroelectric). Ferroelectric PZT undergoes tetragonal and rhombohedral phases for lower and higher content of $PbZrO_3$ respectively[1], and for composition of x=0.48 of Zr there is monoclinic phase below 20K[4]. Structural phase transitions in FE materials can be divided into two different types. If the polarization is discontinuous at the

transition temperature, the transition is called a first-order transition. On the other hand, if polarization is continuous at transition temperature, this type of transition is called a second-order transition. The static dielectric constant near the transition temperature at a second-order transition approximately follows the Curie-Weiss law $\epsilon(0) = C/(T - T_0)$, where C is Curie constant and T_0 is the Curie-Weiss temperature.

Structural phase transitions can also be classified as ferrodistortive and antiferrodistortive classes. In the first class there is no change in the unit cell and in the latter there is a change (doubling the number of atomic bases) of unit cell. According to the soft phonon theory if the optical zone-center phonon freezes at the phase transition temperature and increases above it the transition is ferrodistortive. On the other hand, if the zone-boundary phonons freeze by doubling the unit cell[5], this transition is called antiferrodistortive transition.

Another way to classify the structural phase transitions is order-disorder versus displacive transitions. This classification is mainly based on the microscopic and macroscopic description of the phase transition[1]. In order-disorder transition the energy barrier ΔE between the polar and unpolar states in Fig.1.2 is small, which can be overcome by $k_B T$(shallow double-well potential). In the opposite situation with deep well potential the displacive transition often occurs. There is softmode (temperature dependent mode) only below T_c in an order-disorder transition while in displacive transition there is a finite softmode frequency even above the T_c, which freezes at T_c when approaching from above. Due to the fact that order-disorder and displacive transitions are two extremes cases, most of the phase transitions are no longer purely one type but of mixed type[6]. For example, BTO undergoes mixed transition from cubic to tetragonal phase[7].

1.3 Modern theory of polarization

When a ferroelectric material is placed in a static electric field the induced polarization with respect to applied field follows a hysteresis loop as shown in Fig.1.3. The spontaneous polarization is defined as the dipole moment per unit volume at zero field. In classical electromagnetic theory, the macroscopic polarization is given by

$$\mathbf{P} = \frac{1}{V} \int_V \mathbf{r}\rho(\mathbf{r})d\mathbf{r}, \tag{1.1}$$

where V is the total volume and $\rho(\mathbf{r})$ is the charge density. This conventional theory of polarization by Clausius and Mossotti (CM) is valid only for finite systems where the charge distribution exponentially decays at $r \to \infty$. However, Eq.1.1 couldn't be applied to periodic
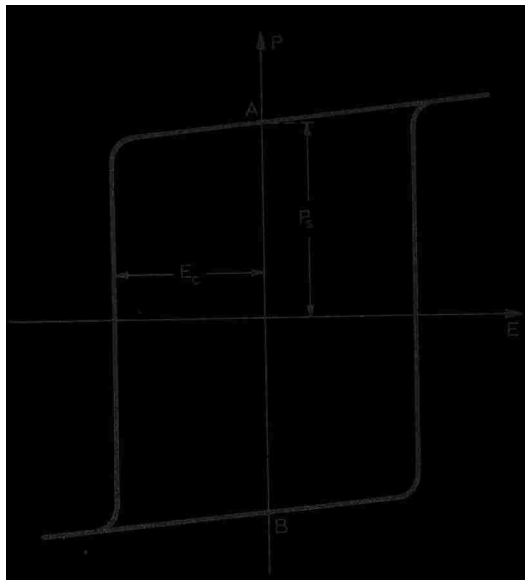
Figure 1.3: A typical hysteresis loop of a ferroelectric material. P_s is the remanent (spontaneous) polarization and E_c is the coercive field and magnitude of AB is the change in polarization to be explained in the text, after [2].

solids for two reasons. First, the charge density $\rho(\mathbf{r})$ in periodic solid does not vanish at $\mathbf{r} \to \infty$, and the integral in Eq.1.1 does not behave properly. Next, the integral in Eq.1.1 depends on the choice of cell due to the fact that the charge distribution in the solid is not localized as in the Clausius and Mossotti model. In order to deal with this limitations of CM theory the quantum theory of polarization was first suggested by Resta[8] and developed by King-Smith and Vanderbilt[9], which assumes that only the change in polarization is physically meaningful. This theory can deal with the problems of periodic system with overlapping charge distributions. In its mathematical formulation the electronic contribution to the change in polarization as shown in Fig.1.3 is given by

$$\Delta \mathbf{P}_e = \int_0^1 \frac{\partial \mathbf{P}_e(\lambda)}{\partial \lambda} d\lambda, \tag{1.2}$$

where λ is the parameter related to the state of polarization ($\lambda = 0$ is initial and $\lambda = 1$ is the final polarized state, points A and B in Fig.1.3). By expanding the Kohn-Sham wavefunction in the parameter space of λ up to the first order and assuming that the change in λ is adiabatically slow, we can write the electronic contribution to the polarization as

$$\mathbf{P}_e(\lambda) = Im \left[\frac{e}{(2\pi)^3} \sum_{n=1}^{M} \int_{BZ} d\mathbf{k} \left\langle u_{n\mathbf{k}}^{(\lambda)} \middle| \nabla_{\mathbf{k}} \middle| u_{n\mathbf{k}}^{(\lambda)} \right\rangle \right], \tag{1.3}$$

where $u_{n\mathbf{k}}^{(\lambda)}$ is the periodic part of the Kohn-Sham wave function, M is the total number of occupied bands and the integral is evaluated over the Brillouin zone. The term in the angle bracket is related to the *Berry connection* or *gauge potential*. The total polarization is the sum of electronic and ionic contributions

$$\mathbf{P} = \mathbf{P}_e^{(\lambda)} + \frac{1}{\Omega} \sum_i e Z_i \mathbf{r}_i, \tag{1.4}$$

where $e Z_i$ is the ionic charge at position $\mathbf{r}_i$. A typical polarization pattern caused by atomic displacements in perovskite oxide is as shown in Fig.1.1

Other useful quantities that can be experimentally accessed and that can be obtained from the knowledge of polarization are the permittivity tensor $\chi_{\alpha\beta}$, pyroelectric coefficient Π_α, piezoelectric tensor $\gamma_{\alpha\beta\delta}$, and dimensionless Born charge tensor $Z^*_{\mathbf{s},\alpha\beta}$ as defined below

$$\chi_{\alpha\beta} = \frac{dP_\alpha}{dE_\beta}, \tag{1.5}$$

$$\Pi_\alpha = \frac{dP_\alpha}{dT}, \tag{1.6}$$

$$\gamma_{\alpha\beta\delta} = \frac{\partial P_\alpha}{\partial\epsilon_{\beta\delta}}, \tag{1.7}$$

$$Z^*_{\mathbf{s},\alpha\beta} = \frac{\Omega}{e}\frac{\partial P_\alpha}{\partial u_{\mathbf{s},\beta}}, \tag{1.8}$$

where α, β and δ are the Cartesian components and E_α is the electric field, T is the temperature, $\epsilon_{\beta\delta}$ is the strain tensor and $\mathbf{u}_\mathbf{s}$ is the displacement of sublattice s.

1.4 Devices and applications

Ferroelectric materials have a wide variety of technological applications due to their special properties. These applications include nonvolatile ferroelectric memories, capacitors, transducers and actuators, ultrasound, sensing and opto-electronic devices, to name only a few of them.

Memories: Ferroelectric materials can be used as a substitute of the volatile (as the power goes off all the data on memory will be lost) dynamic random access memories (DRAM). A data (1 or 0) can be stored as one of the two states of polarization in ferroelectric memory (FeRAM). Ferroelectric materials have spontaneous polarization at the stable ground state so power is not required to retain the data in the memory, which makes the memory non volatile. But in practice while reading the polarization state from the FeRAM it may affect the data from the memory. Other drawbacks of FeRAMs such as the speed of switching polarization, stability of polarization, frequency dependent and size effects are discussed in Ref.[10].
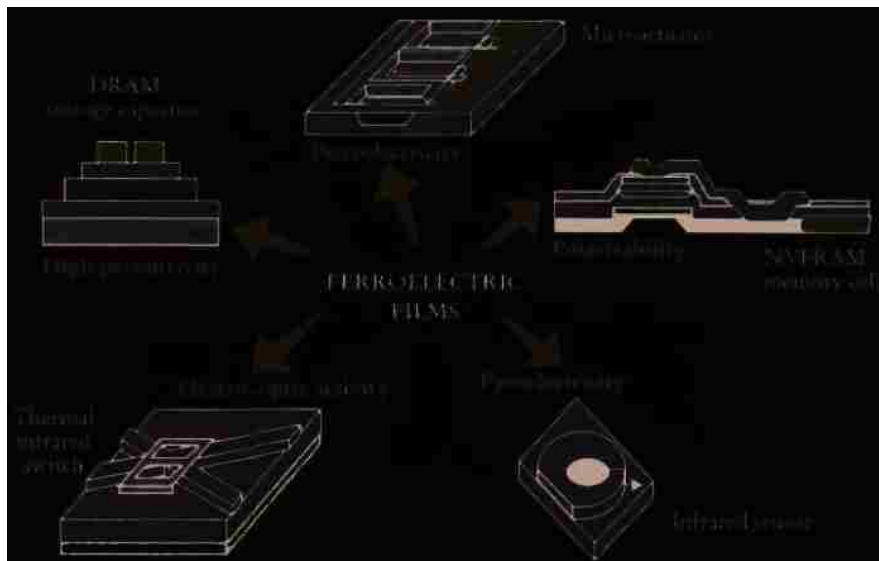
Figure 1.4: Other applications of ferroelectric materials, after [10].

Capacitors: Due to large dielectric constants of FE materials they are suitable candidate to generate large capacitance in a small size. Moreover, due to the nonlinear response of polarization in ferroelectrics these capacitors can be varied with applied voltage, a device known as varactor. Very recent theoretical studies[11, 12] of metal-ferroelectric interface that deal with the tunneling and polarization at the interface are the key factors to further improve the ferroelectric capacitors.
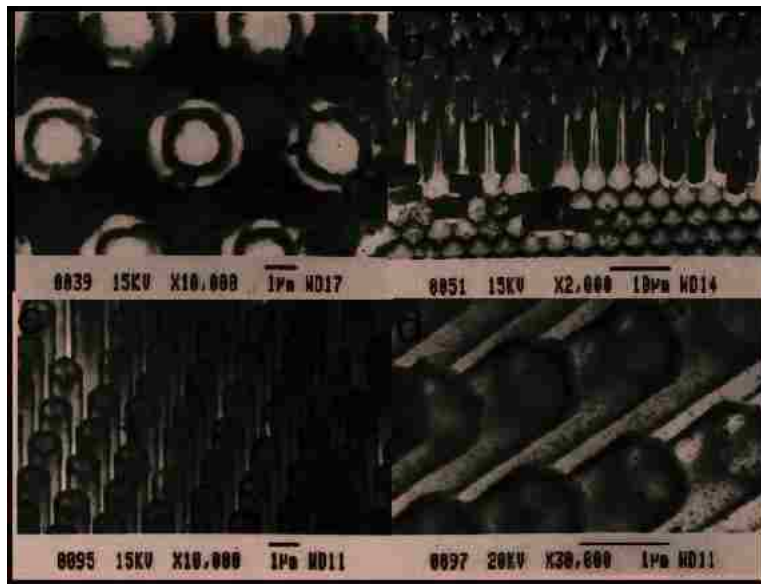
Figure 1.5: Different views of scanning electron microscope image of SBT nanotube array, after [15].

Besides the above applications, Fig.1.4 gives the other possible applications of FE materials as summarized in Ref.[10]. Furthermore, there are a few recent areas of applications. A giant electrocaloric effect on thin film of $PbZr_{0.95}Ti_{0.05}O_3$ is reported in Ref.[13] and this effect may possibly be used in electrical refrigeration. The same material $PbZr_{0.52}Ti_{0.48}O_3$ and BTO can be also made into nanotube array (with tube diameter ranging from 50nm

to several micrometers), which can be utilized in efficient scanner and storage devices[14]. In another experimental work[15] on strontium bismuth tantalate (SBT), free standing nanotube arrays as shown in Fig.1.5 can be used to make random access memory, ink-jet printers and possible future applications for catalyst due to their very large surface to volume ratio.

1.5   Effects of inplane strain

When growing perovskite materials on a substrate there may be a mismatch of inplane lattice constant between substrate and the grown crystal. This leads to the inplane strain defined as $\eta = \dfrac{|a - a_0|}{a_0}$, where a_0 and a are the inplane lattice constants of the bulk and the epitaxially grown crystal. The application of inplane strain changes the interatomic distances in the inplane direction. To balance this strain the out-of-plane lattice constant will change accordingly with a changing c/a ratio than unstrained case, which will alter the polarization of the crystal. Above a certain critical inplane strain in bulk STO it shows ferroelectric off-center displacements along the out-of-plane direction[20, 21]. Other changes caused by inplane strains include transition temperature, dielectric and piezoelectric properties, etc. The choice of substrate and its orientation can be used to tune the inplane strain of grown materials from compressive to tensile. Thus the use of strain can be used to effectively tune the desired FE properties of the materials.
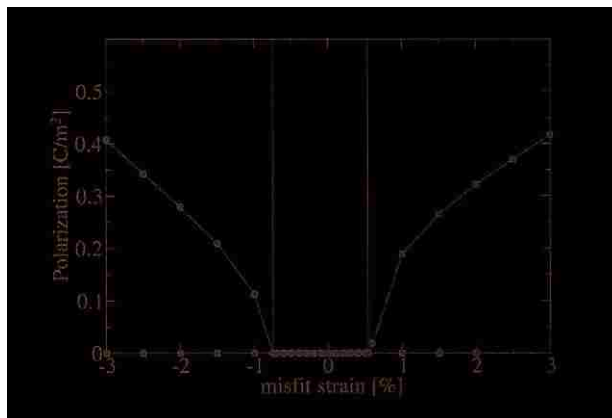
Figure 1.6: Polarization of SrTiO$_3$ with inplane compressive and tensile strains, after [18].

A theoretical work was carried out by Armin Antons *et al.* [18] to study the nonlinear dielectric properties of STO epitaxial film within $\pm 3\%$ of inplane strain. The transition path

from prototype phase of $Pm3m$ symmetry to small compressive or tensile strains leads to the centrosymmetric tetragonal phase of $P4/mmm$ symmetry. This phase later on changes to noncentrosymmetric tetragonal phase of $P4mm$ symmetry along [001] after critical (-0.75%[18] and -0.72%[19]) compressive strain and orthorhombic phase of $Amm2$ symmetry along [110] after critical (+0.54%[18] and +0.83%[19]) tensile strain as shown in Fig1.6.

An experimental work by Haeni *et al.*[20] showed that polarization indeed occur in STO with Curie temperature as high as the temperature under inplane tensile strain of 0.8% by growing STO on DyScO$_3$ oriented along [110] direction. In our calculation of η = -3, -4 and -5% inplane compressive strain we obtained the c/a ratios of 1.061, 1.095 and 1.115 respectively with noncentrosymmetric tetragonal phase and the polarization is along the [001] direction.

1.6 Oxide electronics

Unlike traditional semiconductor electronics of Silicon or III-V materials, Oxide electronics use oxides as active materials for electron transport. Perovskite oxides are one few example and ZnO is another example. Oxide electronics are important mainly because oxides have many novel behaviors as compared to the conventional semiconductors, such as ferroelectricity, ferromagnetism, multiferroics, transparent conductivity, superconductivity, etc[21, 23]. Furthermore, one can combine two different oxides creating an interface, whose properties are very different from those individual oxides. Different symmetry breakings like breaking time-reversal, spatial-inversion, and/or gauge symmetry inversion can happen at the interface, which may lead to novel phenomenon[22], giving rise to technological advantages. The discovery of two-dimensional electron gas[23] (2DEG) at the interface between two insulating oxides $LaAlO_3/SrTiO_3$ (LAO/STO) is one highly acclaimed property in the oxide electronics. Below we discuss some of the few methods to generate the 2DEG for the purpose of oxide electronics.

1.6.1 Heterostructure interface

Both LAO and STO are perovskite oxides with compatible inplane lattice parameters in their bulk cubic form. Experimental lattice constant of LAO from Ref[24] is 3.789Å and for STO is 3.905Å. Our local density approximation (LDA) optimized lattice parameters for LAO and STO are 3.75Å and 3.86Å respectively, which differ by about 1% as compared to the experimental values. So, experimentally LAO can be grown on STO substrate. With experimental growth of an atomic precision LAO/STO superlattice by Ohtomo and Hwang[23] and their finding of free electrons on the interface, people begin to study the origin of 2DEG. Both LAO and STO are insulators with wide bandgaps, but their interface is conducting, which makes the study of heterostructure more interesting. In LAO/STO supercell along the [001] direction, two types of interface can be made: 1) LaO-TiO_2 (also called n-type due to one extra electron from polar $La^{3+}O^{2-}$) interface, and 2) SrO-AlO_2 (p-type due one extra
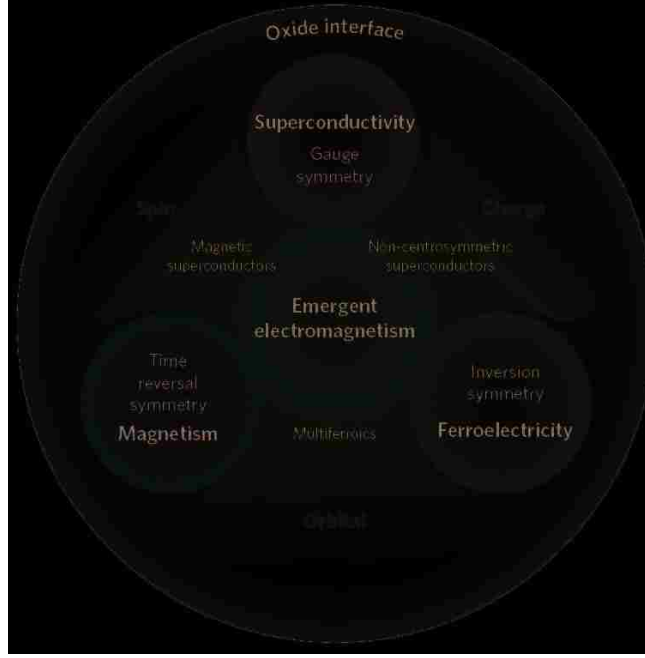
Figure 1.7: different possible phenomena that can happen at oxide interface, after [22].

hole from $Al^{3+}O_2^{2-}$) interface. When growing LAO on STO and making the n-type interface along [001], direction there will be a valence discontinuity at the interface. This leads to half electron per two dimensional unit cell at the interface creating the charge density up to the order of 10^{14} cm^{-2}[25, 26]. There will be an ever increasing Coulomb potential (polar catastrophe) due to the increasing polar layers and Ref[24] suggested that this catastrophe can be avoided by adding half an electron on the single TiO_2 layer at the interface, giving rise to the interface conductance. In another study of insulating behavior of p-type interface between LAO and STO Zhang *et al.*[27] found a very low energy of oxygen vacancy formation that compensates the p-type carriers at the interface.

There are other interface aspects such as lattice relaxation[28, 30, 31], geometry of crystals[32], temperature effects[28] that can change the properties of interface which are

not discussed here. Fig.1.7 shows the different possible novel phenomena that can happen at oxide interface, which arise due to various symmetry breakings. These kinds of collective electronic behaviors cannot be achieved through individual electrons[29]. In a very recent theoretical study of lanthanum vanadate (LaVO$_3$) and STO heterostructure Elias Assmann et al.[33] predicted a very efficient photo-voltaic effect.

1.6.2 Cleavaged surfaces

It is also possible that the 2DEG can be formed at the surface of a single material. Experimental works[34],[35] have shown that vacuum-cleavaged (bare) surface of STO has electron charge density about 10^{14} cm^{-2}. These charges are attributed to the oxygen vacancies, which is supported by theoretical calculations[36]. Since, our work is not directly related to the single surface (but is related to interface), we are not discussing it further.

1.6.3 δ-doping

When an atomic monolayer in a superlattice is replaced by an other species, this is called δ-doping. In microelectronics, δ-doping has become an important approach in designing electronic structures. It was successfully used in semiconductor electronics to create two-dimensional electron gas (2DEG). However, δ-doped interfaces may be treated as a special case of the regular heretostructure interface, but their electronic properties are markedly different such as there is no signature of antiferromagnetic nature in LaO δ-doped STO but it present in regular interface of LTO/STO[24]. There are a few similar properties such as multichannel conduction is found on both cases. In this work we have replaced SrO layer by a LaO layer in an eight-bulk-cells of STO supercell. The successful experimental growth of this system makes the study more exciting. Fig.1.8 shows the scanning transmission electron microscopy (STEM) image of LaO δ-doped n bulk-cells of STO superlattice.

Recently Kim et al.[37] have fabricated the LaO δ-doped SrTiO$_3$ superlattice and found the multichannel conduction with high and low electron mobilities. Despite the fact that
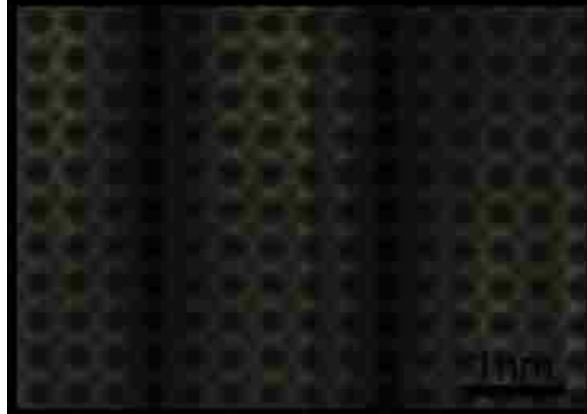
Figure 1.8: Scanning transmission electron microscopy image of LaO δ-doped SrTiO$_3$ supercell, after [25]. The brightest spots are La, medium bright are Sr and dim spots are Ti atoms.

both systems (regular interface and δ-doped) have multichannel conductivity, it is not yet clear about the contributing bands, their precise nature of dispersion and 2D character in the later system. This is one of our objectives to study LaO δ-doped SrTiO$_3$.

It is evident from Section1.5 that the electronic and structural properties will significantly change with the application of homogeneous inplane strain. By combining these effects at the same system as δ-doping makes the properties more interesting and difficult to predict. Our final goal in studying the δ-doped system thus is to study such interplaying effects occurring simultaneously in the same system.

Bibliography

[1] M. E. Lines, and A. M. Glass. *Principles and Applications of Ferroelectrics and Related Materials*, Oxford [Eng.]: Clarendon Press (1977).

[2] E. Fatuzzo, and W. J. Merz, *Ferroelectricity*, Amsterdam: North-Holland Pub. Co (1967).

[3] R. E. Cohen, Nature (London) **358**, 136 (1992).

[4] B. Noheda, D. E. Cox, and G. Shirane, Appl. Phys. Lett., **74**, 2059 (1999).

[5] G. Shirane and Y. Yamada, Phys. Rev. **177**, 858 (1968).

[6] K. A. Muller, H. Thomas, *Structural Phase Transition I*, Berlin: Springer-Verlag (1981).

[7] W. Zong, D. Vanderbilt, and K. M. Rabe, Phys. Rev. Lett., **73**, 1861 (1994).

[8] R. Resta, Theory of electronic polarization in crystals, Ferroelectrics **136**, 51 (1992).

[9] R. D. King-Smith and D. Vanderbilt, Phys. Rev. B **47**, 1651 (1993); D. Vanderbilt and R. D. King-Smith, Phys. Rev. B **48**, 4442 (1993).

[10] O. Auciello, J. F. Scott, and R. Ramesh, Physics Today **51**, 22 (1998).

[11] M. Stengel and N. A. Spaldin, Phys. Rev. B **75**, 205121 (2007).

[12] M. Stengel, D. Vanderbilt and N. A. Spaldin, Phys. Rev. B **80**, 224110 (2009).

[13] A. S. Mischenko, Q. Zhang, J. F. Scott, R. W. Whatmore, and N. D. Mathur, Science **311**, 1270 (2006).

[14] Y. Luo, I. Szafraniak, N. D. Zakharov, V. Nagarajan, M. Steinhart, R. B. Wehrspohn, J. H. Wendorff, R. Ramesh, and M. Alexe, Appl. Phys. Lett. **83**, 440 (2003).

[15] F. D. Morrison, L. Ramsay and J. F. Scott, J. Phys. Condens. Matter **15**, L527 (2003).

[16] A. Antons, J.B. Neaton, K.M. Rabe, and D. Vanderbilt, Phys. Rev. B **71**, 024102 (2005).

[17] Y. Yao and H. Fu, Phys. Rev. B **80**, 035126 (2009).

[18] A. Antons, J. B. Neaton, K. M. Rabe and D. Vanderbild, Phys Rev. B **71**, 024102 (2005).

[19] N. Lihong, L. Yong, S. Chenlu, W. Wei, H. Gaorong and G. Yankai, Physica B **406**, 4145 (2011).

[20] J.H. Haeni,P. Irvin,W. Chang, R. Uecker, P. Reiche, Y. L. Li, S. Choudhury, W. Tian,M. E. Hawley, B. Craigo, A. R. Tagantsev, X. Q. Pan, S. K. Streiffer, L. Q. Chen, S. W. Kirchoefer, J. Levy, D. G. Schlom, Nature (London) **430**, 758 (2004).

[21] J. Heber, Nature (London) **459**, 28 (2009).

[22] H.Y. Hwang, Y. Iwasa, M. Kawasaki, B. Keimer, N. Nagaosa, and Y. Tokura, Nat. Mater. **11**, 103 (2012).

[23] A. Ohtomo, D. A. Muller, J. L. Grazul, and H. Y. Hwang, Nature **419**, 378 (2002); A. Ohtomo and H. Y. Hwang, Nature (London) **427**, 423 (2004).

[24] Z. S. Popovic, S. Satpathy and R. M. Martin, Phys. Rev. Lett. **101**, 256801 (2008).

[25] H.Y. Hwang and A. Ohtomo and N. Nakagawa and D.A. Muller and J.L. Grazul, Physica E **22**, 712 (2004).

[26] J. Lee and A. A. Demkov, Phys Rev. B **78**, 193104 (2008).

[27] L. Zhang, Xiang-Feng Zhou, Hui-Tan Wang, Jing-Jun Xu, J. Li, E. G. Wang, Su-Huai Wei, Phys. Rev. B **82**, 125412 (2010).

[28] D. R. Hamann, D. A. Muller, and H. Y. Hwang, Phys. Rev. B **73**, 195403 (2006).

[29] P. W. Anderson, Science **177**, 393 (1972).

[30] S. Okamoto, A. J. Mills, and N. A. Spaldin, Phys. Rev. Lett. **97**, 056802 (2006).

[31] P. Larson, Z. S. Popovic, and S. Satpathy, Phys. Rev. B **77**, 245122 (2008).

[32] H. Ishida and A. Liebsch, Phys. Rev. B **77**, 115350 (2008).

[33] E. Assmann, P. Blaha, R. Laskowski, H. Karsten, S. Okamoto, and G. Sangiovanni, Phys. Rev. Lett. **110**, 078701 (2013).

[34] A. F. Santander-Syro, O. Copie, T. Kondo, F. Fortuna, S. Pailhs, R. Weht, X. G. Qiu, F. Bertran, A. Nicolaou, A. Taleb-Ibrahimi, P. Le Fvre, G. Herranz, M. Bibes, N. Reyren, Y. Apertet, P. Lecoeur, A. Barthlmy, and M. J. Rozenberg, Nature (London) **469**, 189 (2011)

[35] W. Meevasana, P. D. C. King, R. H. He, S-K. Mo, M. Hashimoto, A. Tamai, P. Songsiriritthigul, F. Baumberger, and Z-X. Shen, Nature Mater. **10**, 114 (2011).

[36] J. Shen, H. Lee, R. Valenti, and H. O. Jeschke, Phys. Rev. B **86**, 195119 (2012).

[37] J. S. Kim, S. S. A. Seo, M. F. Chisholm, R. K. Kremer, H.-U. Habermeier, B. Keimer, H. N. Lee, Phys. Rev B **82**, 201407 (2010).

[38] K.-J. Zhou, M. Radovic, J. Schlappa, V. Strocov, R. Frison, J. Mesot, L. Patthey, T. Schmitt, Phys. Rev. B **83**, 201402 (2011).

[39] A. Joshua, S. Pecker, J. Ruhman, E. Altman, and S. Ilani, Nature Communications **3**, 1129 (2012).

[40] W. Siemons, G. Koster, H. Yamamoto, W. A. Harrison, G. Lucovsky, T. H. Geballe, D. H. A. Blank, and M. R. Beasley, Phys. Rev. Lett. **98**, 196802 (2007).

Chapter 2

Theoretical methods

2.1 Density functional theory

A quantum mechanical system is described by the Schrodinger equation $\hat{H}\Psi = \varepsilon\Psi$, where $\hat{H}$ is the many-body Hamiltonian of the system and Ψ is the many-body wave function. The Hamiltonian of an interacting system of N electrons and M nuclei in atomic units (which we adopt throughout this chapter unless otherwise stated) is

$$\hat{H} = -\frac{1}{2}\sum_i \nabla_i^2 - \sum_I \frac{1}{2M_I}\nabla_I^2 - \sum_{i,I} \frac{Z_I}{|\mathbf{r}_i - \mathbf{R}_I|} + \frac{1}{2}\sum_{i\neq j} \frac{1}{|\mathbf{r}_i - \mathbf{r}_j|} + \frac{1}{2}\sum_{I\neq J} \frac{Z_I Z_J}{|\mathbf{R}_I - \mathbf{R}_J|}. \quad (2.1)$$

The first two terms in Eq.(2.1) are the kinetic energy operators of electron and nuclei respectively. The last three terms are the Coulomb interactions of electron-nuclei, electron-electron, and nuclei-nuclei, respectively. With the consideration that the mass ratio of nucleus to electron is very large, we can simplify Eq.(2.1) using the Born-Oppenheimer approximation, where the electron degrees of freedom and ion degrees of freedom are decoupled. With this approximation, the degrees of freedoms of the nuclei motions are replaced by a constant energy surface. The new Hamiltonian for the electrons looks like

$$\hat{H} = -\frac{1}{2}\sum_i \nabla_i^2 - \sum_{i,I} \frac{Z_I}{|\mathbf{r}_i - \mathbf{R}_I|} + \frac{1}{2}\sum_{i\neq j} \frac{1}{|\mathbf{r}_i - \mathbf{r}_j|} + Const \quad (2.2)$$

In real physical system it is still difficult to solve the many-electron Schrodinger equation even with the Hamiltonian approximated by Eq.(2.2) to obtain the ground-state wave function of electrons and hence the other physical properties. This situation leads one to think about other methods to solve the Schrodinger equation. One such method is the Density Functional Theory (DFT) [1], all the ground-state physical properties of the system of many

interacting electrons can be obtained as a functional of the ground-state density. In pre-DFT era electronic problems were mainly solved by Hartree-Fock theory and its modifications[2], which are based on approximating the many-electron wavefunction by e.g., Slater determinant of single-electron wavefunctions. The main objective of DFT is to replace the many-body electronic wavefunction with the electronic charge density as the basic quantity for the ground-state. The great computational advantage of DFT over Hartree-Fock theory is that there are many single-particle wavefunctions that need to be determined in Hartree-Fock approach while only the charge density needs to be determined in DFT.

2.1.1 Hohenberg-Kohn theorem

Theorem 2.1. *For the interacting non-degenerate electron gas there is one-to-one correspondence between the ground-state charge density and external potential V_{ext} (usually the ionic potential in solids).*

Now consider a different Hamiltonian H' with external potential V'_{ext} and ground-state eigenfunction Ψ' that yields the same charge density $n(\mathbf{r})$ as the ground state. We can establish the following inequality

$$E' = \langle \Psi'|H'|\Psi' \rangle \; < \; \langle \Psi|H'|\Psi \rangle \; = \; \langle \Psi|(H + V'_{ext} - V_{ext})|\Psi \rangle$$

or

$$E' < E + \int (v'_{ext}(\mathbf{r}) - v_{ext}(\mathbf{r}))n(\mathbf{r})d\mathbf{r} \tag{2.3}$$

By using $\langle \Psi|H|\Psi \rangle < \langle \Psi'|H|\Psi' \rangle$, namely interchanging primed and unprimed symbols in Eq.(2.3), we have

$$E < E' + \int (v_{ext}(\mathbf{r}) - v'_{ext}(\mathbf{r}))n(\mathbf{r})d\mathbf{r}. \tag{2.4}$$

Adding Eq.(2.3) and Eq.(2.4), we get

$$E' + E < E + E', \tag{2.5}$$

which is simply not possible. So we must have $V'_{ext} = V_{ext}$.

Theorem 2.2. *The ground-state charge density of the system above can be obtained by minimizing a unique energy functional $E_0 = E[n(\mathbf{r})]$.*

By defining the universal functional $F[n(\mathbf{r})] = \langle \Psi | T + V_{ee} | \Psi \rangle$, then for a given external potential $v_{ext}(\mathbf{r})$ the energy functional is defined as

$$E[n(\mathbf{r})] = F[n(\mathbf{r})] + \int v_{ext}(\mathbf{r})n(\mathbf{r})d\mathbf{r}. \tag{2.6}$$

Suppose there is another density $n'(\mathbf{r})$ and associated state Ψ', then the energy

$$E[n'(\mathbf{r})] = F[n'(\mathbf{r})] + \int v_{ext}(\mathbf{r})n'(\mathbf{r})d\mathbf{r} \tag{2.7}$$

is greater than the ground-state energy that depends on ground-state density $n_0(\mathbf{r})$

$$E[n_0(\mathbf{r})] = F[n_0(\mathbf{r})] + \int v_{ext}(\mathbf{r})n_0(\mathbf{r})d\mathbf{r} \tag{2.8}$$

namely, $E[n'(\mathbf{r})] > E[n_0(\mathbf{r})]$.

Therefore the functional $E[n(\mathbf{r})]$ has its minimum relative to the variations $\delta n(\mathbf{r})$ of the charge density $n_0(\mathbf{r})$, and the ground-state energy is $E = E[n_0(\mathbf{r})] = minE[(\mathbf{r})]$ or
$$\left.\frac{\delta E[n(\mathbf{r})]}{\delta n(\mathbf{r})}\right|_{n(\mathbf{r})=n_0(\mathbf{r})} = 0$$
The energy functional for the interacting electron system can be written as

$$E[n] = T_{int}[n] + V_{ext}[n] + V_{ee}[n] \tag{2.9}$$

where the first and last terms are unknown. To better deal with this problem, one often assumes that the electronic charge density of an interacting electron system can be written

as a sum of single-particle charge density of non-interacting electron gas as

$$n(\mathbf{r}) = \sum_i^N |\phi_i(\mathbf{r})|^2$$

where the sum extends for all occupied states. For a system of non-interacting electrons, the kinetic and electron-electron Coulomb interactions are known exactly. Thus the energy functional will be

$$E[n] = T_{nonint}[n] + V_{ext}[n] + V_H[n] + E_{xc}[n]. \tag{2.10}$$

In Eq.(2.10)

$$T_{nonint}[n] = -\frac{1}{2}\sum_i^N \int \phi_i^*(\mathbf{r})\nabla^2\phi_i(\mathbf{r})d\mathbf{r}, \tag{2.11}$$

$$V_H[n] = \frac{1}{2}\int \frac{n(\mathbf{r}_1)n(\mathbf{r}_2)}{|\mathbf{r}_1 - \mathbf{r}_2|}d\mathbf{r}_1 d\mathbf{r}_2 \tag{2.12}$$

are the kinetic energy and classical Coulomb interaction energy between electrons (or Hartree energy) of a non-interacting system, respectively. E_{xc}, known as *exchange-correlation* energy, is the sum of differences in kinetic energy between interacting and non-interacting electrons as well as the error caused by expressing electron-electron interaction by Hartree energy[3].

$$E_{xc} = T_{int} - T_{nonint} + V_{ee} - V_H \tag{2.13}$$

By minimizing the total energy in Eq.(2.9) with respect to single-particle state ϕ_i, one can obtain a set of Schrodinger-like equations

$$\left[-\frac{\nabla^2}{2} + V_{KS}(\mathbf{r})\right]\phi_i(\mathbf{r}) = \epsilon_i\phi_i(\mathbf{r}), \tag{2.14}$$

known as Kohn-Sham equations, where $V_{KS}(\mathbf{r}) = V_{ext} + V_H + V_{xc}$ is the effective Kohn-Sham potential and $V_{xc} = \dfrac{\delta E_{xc}}{\delta n(\mathbf{r})}$ is the exchange-correlation potential.

Calculation of electronic wave function from Eq.(2.14) is not straightforward since V_{KS}

depends on charge density itself and furthermore E_{xc} is unknown. In order to solve Eq.(2.14) we first approximate the E_{xc} term and solve by self-consistent iterative method.

2.1.2 Local density approximation (LDA)

There are many methods to approximate the E_{xc} term. Here we discuss the local density approximation (LDA)[1], which is valid under the assumption that the density $n(\mathbf{r})$ of interacting system varies slowly in space. The expression for the LDA exchange-correlation energy functional is given by

$$E_{xc}^{LDA}[n] = \int n(\mathbf{r})\epsilon_{xc}^{homo}[n](\mathbf{r})d\mathbf{r}, \tag{2.15}$$

where $\epsilon_{xc}^{homo}[n](\mathbf{r})$ is the exchange-correlation energy per electron in a homogeneous uniform electron gas of the same density $n(\mathbf{r})$ of the considered system at $\mathbf{r}$.

The expression for exchange-correlation energy density is given by Ceperley-Alder[4] as numerical data obtained from quantum Monte Carlo calculation, and later parameterized by Perdew-Zunger[5] and Perdew-Wang[6]. In this work we have chosen the Perdew-Zunger expression. The LDA expressions for E_{xc} can be extended for the spin-polarized systems[7] known as local spin density approximation (LSDA). There are other non-local approximations for E_{xc} functionals as well. One of them is generalized gradient approximation (GGA) which accounts for both the density and its gradient[8].

Despite its many successful predictions on electronic structure calculations local density functional theory has yielded wrong results in strongly correlated electron systems, which we will discuss further in Section2.2.

2.2 LDA+U method

Despite its great success to give the electronic ground state and other related properties, LDA (LDA and/or GGA both) has very limited use to fully describe the strongly correlated electron system with partly filled (and localized) d or f shells (such as Ti and La ions in our study). This type of problem arises in LDA because it does not account for the strong Coulomb repulsion between $3d$ electrons in metal ions[9]. One of the problems with LDA is that it incorrectly predicts a metallic state for transition metal monoxides, while they are insulators[10]. Besides the strongly correlated systems, the well known band gap underestimation in LDA exists because it does not accurately account the full exchange-correlation contribution to the gap[7]. LDA also underestimates the equilibrium lattice constants[11]. One of the many attempts to overcome the LDA problems in strongly correlated systems is to use LDA+U method initially suggested by Anisimov and others[12, 13, 14]. In this method one separates electrons in localized and delocalized orbitals, in which localized electrons (having strong on-site Coulomb interaction e.g. $3d$ orbitals) are treated by Hubbard-like[15] interaction $\frac{U}{2} \sum_{i \neq j} n_i n_j$, where n_i are the orbital occupancy numbers of d orbitals. We deal with delocalized s or p electrons by standard LDA. Since there is already (incorrect) inclusion of direct Coulomb interaction in LDA, this term need to be subtracted from the LDA+U energy functional. Under this situation a simple (neglecting exchange and non-sphericity) LDA+U energy functional would be[12]

$$E = E^{LDA} - \frac{U}{2}N(N-1) + \frac{U}{2} \sum_{i \neq j} n_i n_j \tag{2.16}$$

where $N = \sum_i n_i$ is the total number of d electrons.

By differentiating Eq.(2.16) with respect to orbital occupations n_i

$$\epsilon_i = \frac{\partial E}{\partial n_i} = \epsilon_i^{LDA} + U \left(\frac{1}{2} - n_i \right), \tag{2.17}$$

we can see how this model will change the LDA orbital energy by creating a gap of U between unoccupied ($n_i = 0$) and occupied ($n_i = 1$) orbitals, thereby giving qualitatively correct bandgap in strongly correlated materials.

A further improvement on this functional is to make it rotationally invariant[9, 16, 17]. The modified energy functional looks like

$$E^{LDA+U}[n(\mathbf{r})] = E^{LDA}[n(\mathbf{r})] + E^U[\{n^{I\sigma}_{mm'}\}] - E^{dc}[\{n^{I\sigma}\}] \quad (2.18)$$

where $n(\mathbf{r})$ is the electron density, $\{n^{I\sigma}_{mm'}\}$ are the generalized atomic orbital occupations of the atom at site I with strong on-site Coulomb repulsion, σ is the spin component, m is the magnetic quantum number and $n^{I\sigma} = \sum_m n^{I\sigma}_{mm}$. In Eq.(2.18) The first term is the standard LDA functional, second term represents the Hubbard contribution and the last term is the double counting correction as mentioned earlier. The mathematical forms of these contributions are

$$E^U[n] = \frac{1}{2} \sum_{\{m\},\sigma,I} \left[\langle m_1, m_3 | V_{ee} | m_2 m_4 \rangle n^{I,\sigma}_{m_1,m_2} n^{I,-\sigma}_{m_3,m_4} \right.$$
$$\left. - (\langle m_1, m_3 | V_{ee} | m_2, m_4 \rangle - \langle m_1, m_3 | V_{ee} | m_4, m_2 \rangle) n^{I,\sigma}_{m_1,m_2} n^{I,-\sigma}_{m_3,m_4} \right] and \quad (2.19)$$

$$E^{dc}[n] = \sum_I \left[\frac{U}{2} n^I \left(n^I - 1 \right) - \frac{J}{2} \left(n^{I\uparrow} \left(n^{I\uparrow} - 1 \right) + n^{I\downarrow} \left(n^{I\downarrow} - 1 \right) \right) \right], \quad (2.20)$$

where V_{ee} are the screened Coulomb interaction among d electrons of the same atom. V_{ee} is given in terms of Gaunt coefficients[18] and effective Slater integral (F^k)[19, 20] as

$$\langle m_1, m_3 | V_{ee} | m_2, m_4 \rangle = \sum_k a_k \left(m_1, m_2, m_3, m_4 \right) F^k \quad (2.21)$$

where $0 \le k \le 2l$ and coefficients a_k are given by

$$a_k \left(m_1, m_2, m_3, m_4 \right) = \frac{4\pi}{2k+1} \sum_{q=-k}^{k} \langle lm_1 | Y_{kq} | lm_2 \rangle \langle lm_3 | Y^*_{kq} | lm_4 \rangle. \quad (2.22)$$

Due to the nature of Gaunt coefficients ($\langle lm_1|Y_{kq}|lm_2\rangle$) we only have to evaluate F^0, F^2 and F^4 for $3d$ electrons. U and J are, respectively, the screened onsite Coulomb and exchange energies given by

$$U = \frac{1}{(2l+1)^2} \sum_{m_1,m_2} \langle m_1, m_2|V_{ee}|m_1, m_2\rangle = F^0 \tag{2.23}$$

$$J = \frac{1}{2l(2l+1)} \sum_{m_1,m_2} \langle m_1, m_2|V_{ee}|m_2, m_1\rangle = \frac{F^2 + F^4}{14}. \tag{2.24}$$

The fact that the LDA+U energy functional as obtained above depends on the localized basis sets, and limits the application of this model to the extended systems where the Coulomb and exchange parameters obtained from atomic-like approximation are not valid. In order to generalize the model, Cococcioni and de Gironcoli[21] proposed a simplified scheme which assumes that the higher-order Slater integrals are negligible and the contribution of J is included in U as $U - J$ while preserving the rotational invariance. This model makes the energy functional to be basis set independent so that plane-wave basis set can be used to construct the generalized atomic occupation matrix. The second and last term in Eq.(2.18) are thus modified as

$$E^U \left[\{n_{mm'}^{I\sigma}\}\right] - E^{dc}\left[\{n^{I\sigma}\}\right] = \frac{U}{2} \sum_I \sum_{m\sigma} \left\{ n_{mm}^{I\sigma} - \sum_{m'} n_{mm'}^{I\sigma}, n_{m'm}^{I\sigma} \right\}. \tag{2.25}$$

It is clear from Eq.(2.25) that U in the equation is a parameter. In our work this quantity is obtained by fitting the theoretical band gap with the experimental result. In Ref. [21] there is a robust way to calculate U by a linear response method which will not be discussed here.

2.3 Pseudopotentials

To solve the Kohn-Sham equation in solid, one often expands the single-particle wavefunctions in terms of planewave basis. Due to the wiggling nature of core electrons, expressing them in planewaves requires a extremely large number of basis sets. Since core electrons are mostly localized to ion and are less important determining physical and chemical properties of the material, they can be considered as external effective potential for the valence electrons. However, classification of valence and core electrons on certain atoms may not be straightforward. Thus the pseudopotential method equivalently transforms the all-electron problem into valence-electrons only problem.

There are different methods in literatures [22]-[26] to generate the pseudopotential but they are similar in basic principles. Below we will discuss some of the first-principles approaches to generate the pseudopotentials.

2.3.1 Norm-conserving pseudopotentials

First-principles pseudopotentials are generated by solving all-electron radial Kohn-Sham equation within the density functional theory

$$\left[-\frac{1}{2}\nabla^2 + \frac{l(l+1)}{2r^2} + V^{KS}(r) \right] \psi_l^{AE}(r) = \epsilon_l \psi_l^{AE}(r) \tag{2.26}$$

where $V^{KS}(r) = V_{ext} + V_H[n(r)] + V_{xc}^{LDA}[n(r)]$ is the self-consistent, one-electron potential with V_{xc}^{LDA} being the exchange correlation potential within LDA, and $\psi_l^{AE}(r)$ is the atomic radial wave function for angular momentum l.

We then replace the atomic wavefunction ψ_l^{AE} by a pseudowavefunction ψ_l^{PS} within the pseudization radius of $r_{c,l}$, which will satisfy the following conditions[22]

- Pseudowavefunction ψ_l^{PS} contains no nodes.

-
$$\psi_l^{PS} = \begin{cases} \psi_l^{AE} & \text{if } r > r_{c,l} \\ \\ r^{l+1} f(r) & \text{if } r \leq r_{c,l} \end{cases} \tag{2.27}$$

- Norm conserving, i. e. $\int_0^{r_{c,l}} |\psi_l^{PS}|^2 r^2 dr = \int_0^{r_{c,l}} |\psi_l^{AE}|^2 r^2 dr$

- Pseudopotential eigenvalue ϵ_l^{PS} = all-electron eigenvalue ϵ_l^{AE}

Here, $f(r) = \sum_{i=0}^{12} c_i r^i$ for even i only is the Troullier-Martin's method[23]. This method is an improved version of Kerker[22] and mostly focus on the smoothness of pseudopotential. The coefficients c_i are calculated with norm conserving condition, continuity of $\psi_l^{PS}(r)$ and its derivatives up to the fourth order at $r_{c,l}$, and zero curvature of screened pseudopotential at the origin.

Another advance in generating pseudopotential is due to Rappe and others (RRKJ)[24]. In RRKJ pseudization the optimized pseudowavefunction is expressed as a sum of Bessel functions instead of polynomial as in Ref [23], which is equal to all-electron wavefunction outside the cutoff radius r_c and $f(r) + c(r)$ inside $r \leq r_c$. The expression for $f(r)$ is given below

$$f(r) = \sum_{i=1}^{3(4)} \alpha_i j_l(q_i r) \tag{2.28}$$

where the coefficients α_i and parameters q_i are found from normalization condition and the continuity conditions between pseudo-wavefunction and $\phi_l^{AE}(r)$ at $r = r_{c,l}$. $c(r)$ is also the sum of Bessel functions whose coefficients are chosen to minimize the kinetic energy beyond q_c and it vanishes at r_c.

Once the pseudo-wavefunction is determined as above, we invert the Schrodinger equation to obtain the screened (mixed with Hartree and exchange correlation potential) pseudopotential as follows

$$V_l^{scr}(r) = \epsilon_l - \frac{l(l+1)}{2r^2} + \frac{1}{2\psi_l^{PS}(r)} \frac{d^2 \psi_l^{PS}(r)}{dr^2}. \tag{2.29}$$

Once we remove the Hartree and exchange-correlation part from Eq.(2.29), we obtain the ionic pseudopotential. Pseudopotential thus generated is called norm conserving pseudopotential (NC-PP).

2.3.2 Ultrasoft pseudopotential (USPP)

In norm conserving pseudopotential it is difficult to deal with highly localized orbitals such as $2p$ in first row atoms, $3d$ in transition metal atoms and $4f$ in rare-earth atoms due to very large number of planewave basis sets. This difficulty can be overcome by relaxing the direct norm-conserving condition inside the cutoff radius r_c[26]. This will allow one to choose the larger cutoff radius than used in NC-PP. To achieve such condition the valence charge density is compensated by an augmented charge density in the self-consistent calculation.

The pseudowavefunction in this method is the solution of generalized eigenvalue problem.

$$\mathbf{H} \left| \psi_{n,\mathbf{k}}^{PS} \right\rangle = \epsilon_{n,\mathbf{k}} \mathbf{S} \left| \psi_{n,\mathbf{k}}^{PS} \right\rangle \tag{2.30}$$

where $\mathbf{H}$ is the usual Hamiltonian and $\mathbf{S}$ is the non-local overlap operator, which orthonormalize the pseudowavefunction as below

$$\left\langle \psi_{n,\mathbf{k}}^{PS} \left| \hat{S} \right| \psi_{n',\mathbf{k}}^{PS} \right\rangle = \delta_{n,n'} \tag{2.31}$$

The form of operator $\mathbf{S}$ is given by

$$S = 1 + \sum_{i,j} Q_{i,j} \left| \beta_i \right\rangle \left\langle \beta_j \right| \tag{2.32}$$

where β_i are the constructed local functions from $\psi_i^{PS}(r)$, the matrix $Q_{i,j} = \psi_i^{*AE}(r)\psi_j^{AE}(r) - \psi_i^{*PS}(r)\psi_j^{PS}(r)$, which relax the direct norm conserving condition. This kind of pseudopotential must be updated at each self-consistent iteration.

Bibliography

[1] P. Hohenberg and W. Kohn, Phys. Rev. **136**, B864 (1964); W. Kohn and L. J. Sham, Phys. Rev. **140**, A1133 (1965).

[2] M. Born and J. R. Oppenheimer, Ann. Physik **84**, 457 (1927); J. Slater, Phys. Rev. **34**, 1293 (1929).

[3] R. O. Jones and O. Gunnarsson, Rev. Mod. Phys. **61**, 689 (1989)

[4] D. M. Ceperly and B. J. Alder, Phys. Rev. Lett. bf 45, 566 (1980).

[5] J. P. Perdew and A. Zuner, Phys. Rev. B **23**, 5048 (1981).

[6] J. P. Perdew and Y. Wang, Phys. Rev. B **45**, 13244 (1992).

[7] C. Fiolhais, F. Nogueira and M. Marques (Eds.), LPN **620**, pp. 1-55 (2003).

[8] J. P. Perdew, K. Burke and M. Ernzerof, Phys. Rev. Lett. **77**, 3865 (1996).

[9] S. L. Dudarev, G. A. Botton, S. Y. Savrasov, C. J. Humphreys, and A. P. Sutton, Phys. Rev. B **57**, 1505 (1997).

[10] K. Terakura, T. Oguchi, A. R. Williams and J. Kübler, Phys. Rev. Lett. **52**, 1830 (1984).

[11] O. K. Andersen, H. L. Skriver, H. Nohl, and B. Johansson, Pure Appl. Chem. **52**, 93 (1980).

[12] V. I. Anisimov, J. Zaanen, and O. K. Andersen, Phys. Rev. B **44**, 943 (1991).

[13] V. I. Anisomov, I. V. Solovyev, M. A. Koroton, M. T. Czyzyk, G. A. Sawatzky, Phys. Rev. B **48**, 16929 (1993).

[14] I. V. Solovyev, P. H. Dederichs, V. I. Anisimov, Phys. Rev. B **50**, 16861 (1994).

[15] J. Hubbard, Proc. R. Src. London, Ser. A **276**, 238 (1963); **277**, 237 (1964); **281**, 401 (1964).

[16] A. I. Liechtenstein, V. I. Anisimov, and J. Zaanen, Phys. Rev. B **52**, R5467 (1995).

[17] V. I. Anisimov, F. Aryasetiawan and A. I. Lichtenstein, J. Phys.: Condens. Matter **9**, 767 (1997).

[18] J. A. Gaunt, Phil. Trans. Royal Soc. London A, **228**, 151 (1929).

[19] V. I. Anisimov and O. Gunnarsson, Phys. Rev. B **43**, 7570 (1990).

[20] B. R. Judd, *Operator Techniques in Atomic Spectroscopy*, Princeton University press, 1998.

[21] M. Cococcioni and S. de Gironcoli, Phys. Rev. B. **71**, 035105 (2005).

[22] G. P. Kerker, J. Phys. C **13**, L189 (1980).

[23] N. Troullier and J. L. Martim, Phys. Rev. B **43**, 1993 (1991).

[24] A. M. Rappe, K. M. Rabe, E. Kaxiras and J. D. Joannapoulos, Phys. Rev. B **41**, 1227 (1989).

[25] D. R. Hamann, Phys. Rev. B **40**, 2980 (1989).

[26] David Vanderbilt, Phys. Rev. B **41**, 7892 (1990).

Chapter 3

Ferroelectric Pb(Zr$_{0.5}$Ti$_0$.5)O$_3$ (PZT) nanotube array

3.1 Introduction

Nanostructures made of ferroelectrics (FEs) have attracted widespread attention because these FE nanostructures often lead to new physics and new phenomena that may not exist in bulk materials.[1, 2] Examples include the growth of FE artificial superlattices[3] where enhanced polarization was found in nonferroelectric component[4] and where composition-induced symmetry breaking may destroy ferroelectric double well[5], the existence of critical thickness of FE monodomain[6], FE thin films in which FE stripe domains occur[7, 8, 9] and in which an out-of-plane polarization was shown possible even for thickness of two unit cells[10], FE spherical Pb(ZrTi)O$_3$ and BaTiO$_3$ nanoparticles[11, 12] where a vortex phase was predicted[13], and FE nanowires[14] where phase transition exists in one-dimensional systems[15, 16, 17, 18].

Recently another class of novel FE nanostructures have been fabricated, namely the arrays of ferroelectric nanotubes[19, 20]. Furthermore, different FE materials including Pb(ZrTi)O$_3$, BaTiO$_3$, and SrBi$_2$Ta$_2$O$_9$ were made into the form of nanotube arrays[19, 20], showing that this novel nanostructure is generally applicable to various FE solids. FE nanotube arrays are interesting from both fundamental and technological points of view. Fundamentally, unlike zero-dimensional (0D) nanodots where depolarization field exists in all three directions, FE tubes do not have a depolarization field along the tube axis, thereby dipoles are expected to have different structural properties. Furthermore, unlike one-dimensional (1D) FE wires where long-range dipole interaction is truncated along the lateral directions, nanotube arrays allow long-range interaction along the lateral directions due to the formation of array, which makes the structural phases more subtle and interesting. Technologically,

compared to carbon and BN nanotubes[21, 22], FE nanotubes exhibit superior dielectric and piezoelectric responses, which promise important applications on low-dimensional actuators, MEMS devices, phase shift antenna, and nano-capacitors.[23, 24, 25] Also, differing from an assembly of disordered nanodots, FE nanotube arrays possess a lattice-like structure repetition and are better suitable for nonvolatile FE memories since individual unit can be conveniently addressed[26].

As another intriguing possibility, the properties of FE nanotube arrays can be further tuned by filling the void space outside tubes with matrix medium (which can be either liquids or solid powders). The matrix medium, which may have different polarization magnitude (i.e., different ferroelectric strength) than the tube material itself, plays a critical role in determining the ferroelectric properties of tube array for the following reason. It is known that the properties of FE nanostructures are mainly governed by depolarization field. For instance, depolarization field is responsible for the existence of critical thickness of FE monodomain[6], and it also leads to the vortex phase in FE nanoparticles[13], and moreover, it is depolarization field that forces the polarization in FE nanowires to prefer along the wire axis[15, 16, 17, 18]. Therefore, by altering the depolarization field along the lateral directions (perpendicular to the tube axis), matrix medium in FE nanotube array may lead to new phenomena and/or properties. Although FE properties of *nanodots* in a matrix medium were known[27], these properties obviously cannot apply to FE nanotubes due to the above-described drastic difference between nanodots and nanotubes in terms of depolarization field—namely, there are strong depolarization fields along all three directions in nanodots, but there is no depolarization field along the axis direction in nanotubes.

Despite the fundamental and technological relevance of FE nanotube arrays, theoretical understanding of these arrays is scare. Therefore, any theoretical studies will be useful in terms of exploring this novel class of FE nanostructures. One important issue centers on the structural phases and ferroelectric properties. It is not clear what structural phases the dipoles in the nanotube array may form. We may also wonder whether any new structural

phase may exist in tube array but not in bulk. Furthermore, when the ferroelectric strength of matrix medium varies, the lateral depolarization field in tube array is to change. How does this change affect the structural phases and FE properties? Here it worths pointing out that determination of ordered structural phases in FE nanostructures is a subject of fundamental relevance since phase transition (or dipole ordering) in systems of reduced dimension has been a topic of profound interest for decades.[28, 29, 30] Further, the dipole ordering and/or phase transition in FEs are caused by the delicate balance of various interactions.[31, 32] Determination of structural phases can thus also reveal valuable knowledge on the balance of fundamental interactions.

Another interesting question concerns how an ordered structural phase is *nucleated* in the beginning and then how it subsequently evolves in FE tube array. This question is of general interest since nucleation on nanoscale is an important process which reflects the tipping point of a new balance of interaction. But nucleation process on nanoscale FEs remains largely unknown. While *macroscopic* order parameters such as the magnitude and/or direction of total polarization are very useful in identifying an ordered phase, they nevertheless reveal little knowledge about how the ordered phase is nucleated on the atomic scale. In contrast, obtaining *microscopic* insight into the behaviors of individual dipoles becomes critical in terms of understanding the nucleation process, which is another aim of this study (in addition to determination of structural phases).

Here we determine the structural phases and polarization properties of $Pb(Zr_{0.5}Ti_{0.5})O_3$ nanotube array using first-principles derived effective Hamiltonian and finite temperature Monte Carlo simulations. To investigate how the structural properties are influenced by depolarization field along the lateral directions, we embed the PZT tubes in a matrix medium with a wide range of ferroelectric strengths covering from strongly ferroelectric, to moderately and weakly ferroelectric, to paraelectric. We find that rich structural phases exist in FE tube array, including an unusual phase which has not been reported before (to the best of our knowledge). This unusual phase is characterized by the coexistence of a linear

polarization and a circular polarization. Our simulations also show that another interesting dipole structure of *half vortex* plays an important role in the nucleation process in FE tube array. Furthermore, although the tetragonal polarization phase can be found both in bulk PZT [33] and in PZT tube array at low temperatures, they nevertheless have drastically different phase formation paths, revealing a profound difference in terms of interactions in two systems.

3.2 Theoretical methods

We use temperature-annealing Monte Carlo (MC) simulations to determine the amplitudes and orientations of local dipoles in the tube array. Temperature-annealing MC simulation is a reliable approach to find the most probable state at a given temperature. Most of our simulations start at a high temperature ($\sim$2000K) with initial dipoles in the system randomly oriented, and then the system is gradually cooled down to low temperatures by steps of 50K. Since scientists are often interested in the ground state at low temperature, we will thus first present the structural phases at a low and scaled temperature 64K. Nevertheless, we will also examine high-temperature structural phases.

The total energy of the system is calculated by using a first-principles derived effective Hamiltonian[34, 35], in which the energy E_{tot} depends on local mode $\mathbf{u}_i$ at site i, inhomogeneous strain $\mathbf{v}_i$, homogeneous strain η, and atomic specie σ_i in the alloy. More specifically, the Hamiltonian consists of six terms

$$
\begin{aligned}
E_{\text{tot}} &= E_{\text{on}}(\{\mathbf{u}\}) + E_{\text{sr}}(\{\mathbf{u}\}) + E_{\text{dip}}(\{\mathbf{u}\}) + E_{\text{els}}(\{\eta\}, \{\mathbf{v}\}) \\
&+ E_{\text{els-m}}(\{\mathbf{u}\}, \{\mathbf{v}\}, \{\eta\}) + E_{\text{alloy}}(\{\mathbf{u}\}, \{\mathbf{v}\}, \{\sigma\}, \{\eta\}),
\end{aligned}
$$

which include the on-site energy E_{on} of local modes, short-range interaction energy E_{sr} between neighboring local modes, long-range dipole-dipole interaction energy E_{dip}, elastic energy E_{els} of homogeneous and inhomogeneous strains, elastic-mode coupling energy $E_{\text{els-m}}$, and the energy term E_{alloy} due to alloying, respectively. The expression of each term was given in the literature,[34, 36] and shall not be repeated here. The effective-Hamiltonian approach has been very successful in terms of predicting correct sequences of different phase transitions[34, 35, 36], determining dielectric and piezoelectric coefficients[37], and even yielding accurate transition temperatures after zero-point quantum motion is included[38]. The long-range dipole-dipole interaction is calculated using a periodic Green's-function approach implemented in dual space[16, 39].

The array of PZT nanotubes is simulated using periodically arranged supercells; one supercell is schematically shown in the inset of Fig.3.2. Let a_0 be the lattice constant of a pseudocubic cell of bulk PZT (a_0=7.56 Bohr). The inside radius r_1 of the PZT tube is $5a_0$, and the outside radius r_2 is $10a_0$. The size of the supercell is $31a_0 \times 31a_0 \times 12a_0$. Our simulation results do not sensitively depend on the sizes of r_1, r_2 and supercell when these sizes change by $\pm 50\%$. The tube material between r_1 and r_2 is PZT (i.e., the shaded area in the inset of Fig.3.2), while the void space outside the tube (i.e., the unshaded area in the inset of Fig.3.2) is filled with matrix medium. Unlike the case of bending a FE slab into a tube (in which strain gradient could be large), the nanotube arrays synthesized in experiments[19, 20] are obtained by wetting polymer precursors where there are little *external* strain and/or strain gradient. Therefore, flexoelectricity caused by external strain gradient[40] is not considered here.

The effective Hamiltonian and parameters for the tube material PZT were well documented [35, 36], and have been successfully used to study various PZT nanostructures, including PZT films, nanodisks, and nanowires surrounded by vacuum [8, 13, 16]. We thus mainly discuss the parameters of the matrix material. As described in Sec.3.1, the uttermost important function of the matrix medium is to change the lateral depolarization field in the tube array by varying its ferroelectric strength, since the depolarization field is the predominant key factor that determines the structural properties in FE nanostructures [8, 43]. We have performed various calculations by changing different parameters of the matrix medium, and we found that the most important quantity that controls the ferroelectric strength (or equivalently, polarization magnitude) of the matrix medium is the κ_2 quantity in the on-site energy

$$E_{\text{on}}(\mathbf{u}_i) = \kappa_2 u_i^2 + \alpha u_i^4 + \gamma(u_{ix}^2 u_{iy}^2 + u_{iy}^2 u_{iz}^2 + u_{iz}^2 u_{ix}^2), \tag{3.1}$$

where E is in units of Hartree, and u_i in units of a_0. In this study, κ_2 is varied from 0.18 to 3.18 to mimic different matrix media with different ferroelectric strengths; all κ_2s in this paper are in units of 10^{-2} Hartree. While we have also changed other parameters of

37

the matrix medium, we find that our results are less sensitive to the change of these other parameters. For instance, for a given κ_2 of the matrix medium, we vary other parameters by $\pm 20\%$, and very little changes are found to the structural phases in FE tube array.

The magnitude of polarization and dielectric susceptibility of the matrix medium are given in Fig.3.1 for different κ_2. We see in Fig.3.1 that the considered matrix medium covers a wide range of different possibilities, including strongly ferroelectric with a large polarization $P \geq 0.7\text{C/m}^2$ (such as PbTiO$_3$), moderately FE with $P \sim 0.5\text{C/m}^2$ (such as the recently found material Bi$_{4-x}$Nd$_x$Ti$_3$O$_{12}$ [41]), weakly FE with $P \sim 0.3\text{C/m}^2$ (such as BaTiO$_3$), incipient-like FE with no polarization but with large χ_{33} (such as SrTiO$_3$), and strongly paraelectric with zero polarization and small χ_{33}.
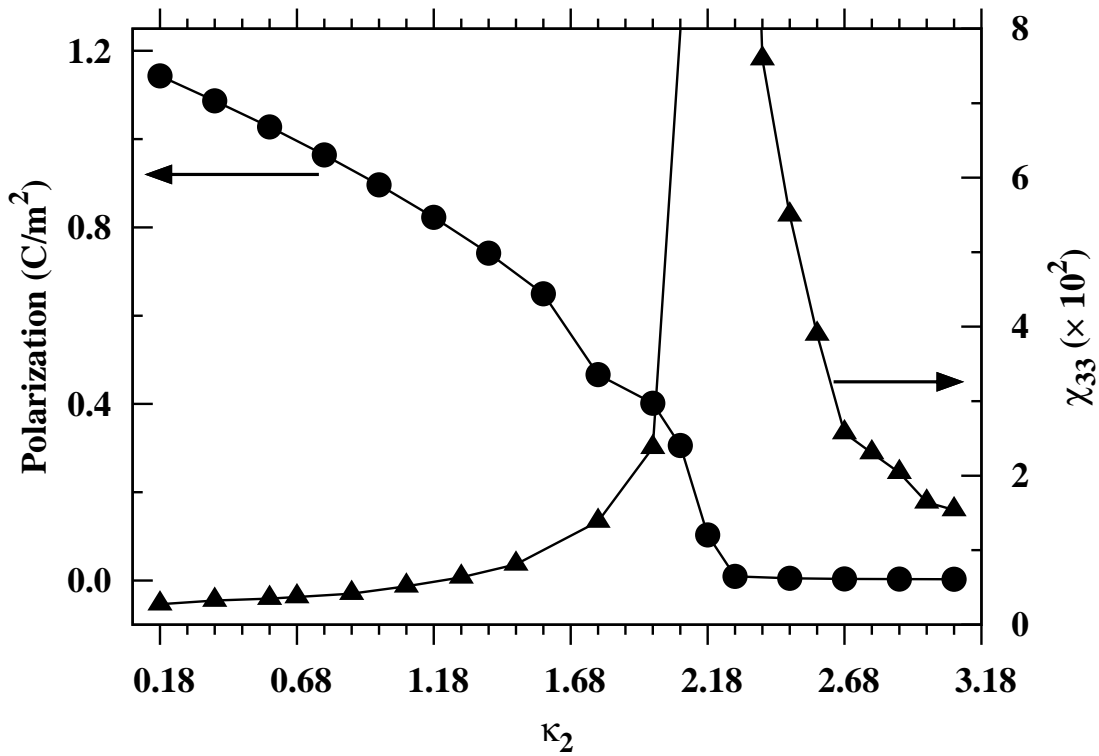
Figure 3.1: Magnitude of polarization (solid dots, using the left vertical axis) and dielectric susceptibility (solid triangles, using the right axis) at 64 K as a function of κ_2 for the matrix material.

Vacuum as a matrix medium is also included in this study. Two different approaches are used to handle vacuum as a matrix medium. The first is to constrain the dipoles in the vacuum to be identically zero, as previously implemented in PZT nanodisks [13]. Another approach is to consider a very large κ_2 ($\sim$10), where our simulations yield practically zero dipole magnitude and no dipole-dipole interaction in the vacuum. Two different approaches give almost identical results. In fact, we find that the structural phase of the PZT tube array embedded in vacuum is very similar to the one which we will show below for $\kappa_2 = 2.18$. We will thus not discuss separately the vacuum-surrounded PZT tube array. The similarity in the structural phases between $\kappa_2 = 10$ and $\kappa_2 = 2.18$ is easy to understand: when κ_2 is sufficiently large, the dipole magnitudes in the matrix are very small, and the matrix behaves like vacuum.

We are aware that our handling of the matrix medium is simplified in the sense that we vary only the κ_2 quantity of the matrix. While κ_2 is indeed the most important quantity to control the depolarization field, other parameters may also play some (although less important) role. Nevertheless, we believe that the key structural phases and properties predicted in this study will not alter, as indeed proved by varying other parameters in our simulations. Importantly, the current approach already yields many unusual properties and interesting physics in FE nanotube arrays, for example, we predict a spontaneous phase transition between vortex and polarization by temperature alone, without the need of any external electric field. More accurate handling of the matrix will make the interesting physics even richer. Considering that there are few theoretical understandings currently available on FE nanotube arrays, we believe that the current study will stimulate more interest in this novel class of FE nanostructures.

3.3 Results and discussions

3.3.1 Low-temperature structural phases

Figure 3.2 shows the three components of the net polarization $< \mathbf{P} >$ of the whole system at 64K as a function of κ_2 of the matrix medium, where $< \mathbf{P} >= \frac{1}{N\Omega} \sum_i z^* \mathbf{u}_i$ (in which i is the site index, N the total number of sites, z^* the effective charge of local mode, and Ω the volume of bulk cell). One important conclusion is ready in Fig.3.2 by contrasting the $< \mathbf{P} >$ polarizations at κ_2=0.88 and κ_2=2.18. At κ_2=0.88, P_z is large and around $\sim$0.9 C/m^2, whereas at κ_2=2.18 all three components of $\mathbf{P}$ are small. The contrast thus shows that (i) matrix medium can drastically modify the polarization in the tube array. Another key outcome in Fig.3.2 is that (ii) the polarization displays interesting discontinuities at two κ_2 values marked by the dashed lines. In addition, the polarization also shows very different κ_2-dependent slopes at the two sides of each dashed line. The discontinuities in Fig.3.2 naturally define three distinct structural phases of different polarization properties, which are described in the following.

When κ_2 is between 0.88 and 1.88, polarization in Fig.3.2 shows two features: (i) For each κ_2, only one polarization component is nonzero while the other two components vanish. (ii) The nonzero component can be P_x, or P_y, or P_z at different κ_2, namely the polarization does not have strong preference among the x, y and z directions. These features reveal that the structural phase is ferroelectric with tetragonal symmetry, which will be denoted as "phase I". The reason for the occurrence of this phase is simple and can be intuitively understood as the following. For the considered range of κ_2, the matrix medium is moderately ferroelectric, resembling PZT. As a result, the lateral depolarization field between tube and matrix is small, and thus the tube array prefers to be ferroelectric with polarization.

One may find it less intuitive that $\mathbf{P}$ changes its direction from one κ_2 to the next in phase I of Fig.3.2. The correct understanding is the following. Take $\kappa_2 = 1.38$ as an example: although the simulation result in Fig.3.2 yields a polarization along the x direction, the

40

polarization nevertheless can also point at the y or z direction with nearly equal probability. To check this, we have performed many other calculations for the same $\kappa_2 = 1.38$, but with different initial (random) dipole configurations, and found that polarization indeed also points at y or z directions, similar to the fact that polarization in tetragonal bulk PbTiO$_3$ can point at six equivalent directions. Since for each κ_2 in phase I, temperature-annealing simulations are performed *independently*, all starting at high temperatures, the calculation result that polarization points at different directions at different κ_2 in phase I demonstrates the equivalence among the x, y, and z directions that are comparably preferable by the polarization. It also is an indication that the system is ergodic.
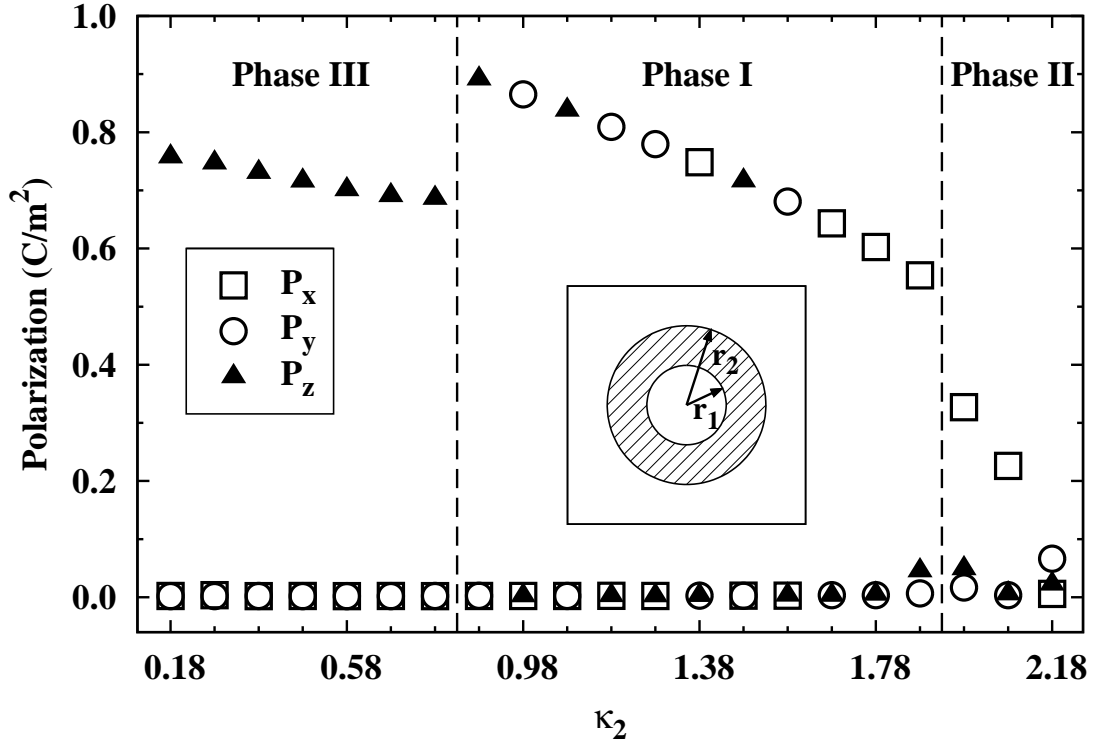
Figure 3.2: Net average polarization of the PZT tube array at 64 K as a function of κ_2. κ_2 is in units of 10^{-2} Hartree. In the inset, the top view (i.e., a cross-section on the xy plane) of one supercell is shown schematically. The tube-axis direction (i.e., the z-axis) is perpendicular to the plane shown in the inset. The shaded area is the PZT tube and the unshaded areas are the void space to be filled with matrix medium.

41

However, as κ_2 is increased above 1.88, new phenomena occur in Fig.3.2. More specifically, besides the polarization discontinuity at κ_2=1.93, (i) P declines much faster with the increasing κ_2 than in phase I; (ii) Polarization at different κ_2 prefers to be along either x or y (but not z) direction, unlike phase I whose $\mathbf{P}$ at different κ_2 may point at any of the three directions; (iii) At κ_2=2.18, all three polarization components vanish rather mysteriously. We have performed additional calculations for other κ_2 ranging from κ_2=2.28 to κ_2=10, showing that the structural phase remains the same as κ_2=2.18. These polarization behaviors, which are obviously incompatible with those of phase I, suggest the existence of a different structural phase (which will be called "phase II"). Result (ii) of phase II is interesting since it reveals a symmetry breaking among the x, y and z directions. It also suggests that the system undergoes a crossover from 3D-like in phase I (where $\mathbf{P}$ can point at all three directions) to 2D-like in phase II (where $\mathbf{P}$ prefers only to be within the xy plane).

The disappearance of $\mathbf{P}$ at $\kappa_2 = 2.18$ is rather unexpected. To investigate this further, we depict in Fig.3.3 the magnitudes of local mode $< u^2 >= \frac{1}{N} \sum_i |\mathbf{u}_i|^2$ inside the tube and inside the matrix, separately. Note the key difference between $< \mathbf{u} >$ and $< u^2 >$: while vector $< \mathbf{u} >$ may vanish if $\mathbf{u}_i$s of different sites point at opposite directions, $< u^2 >$ does not. Fig.3.3 reveals that with the increase of κ_2, $< u^2 >$ in the matrix decreases in a rather linear fashion, but $< u^2 >$ in the tube changes only slightly. In particular, $< u^2 >$ in the tube does not vanish at $\kappa_2 = 2.18$ and its magnitude is in fact close to that in phase I (see the solid dots in Fig.3.3), demonstrating that individual dipoles in the tube remain large in phase II. Since the depolarization field along the z-axis is zero, common wisdom tells that dipoles in the tube at $\kappa_2 = 2.18$ should be aligned along the tube-axis direction, forming a nonzero z-axis polarization in phase II. Surprisingly, this z-axis polarization does not occur in phase II.

When κ_2 is below 0.83, another interesting structural phase (phase III) occurs in Fig.3.2. Unlike phase I where $\mathbf{P}$ can point at any of the three directions and the system is 3D-like, polarization in phase III prefers only the z-axis direction for different κ_2 and the system be-

haves 1D-like. Furthermore, unlike phase I where the magnitude of polarization $|\mathbf{P}|$ *increases* as κ_2 decreases, $|\mathbf{P}|$ undergoes a sudden and anomalous *decrease* from κ_2=0.88 to κ_2=0.78 at the boundary between phases I and III. This sudden decrease in $|\mathbf{P}|$ is very puzzling, and the underlying origin will be investigated in the next section. Combining the results of all three phases, we thus see that by varying κ_2 the system can transition from 3D-like (phase I), to 2D-like (phase II), to 1D-like (phase III), which is an effective route to tune the properties of the system.
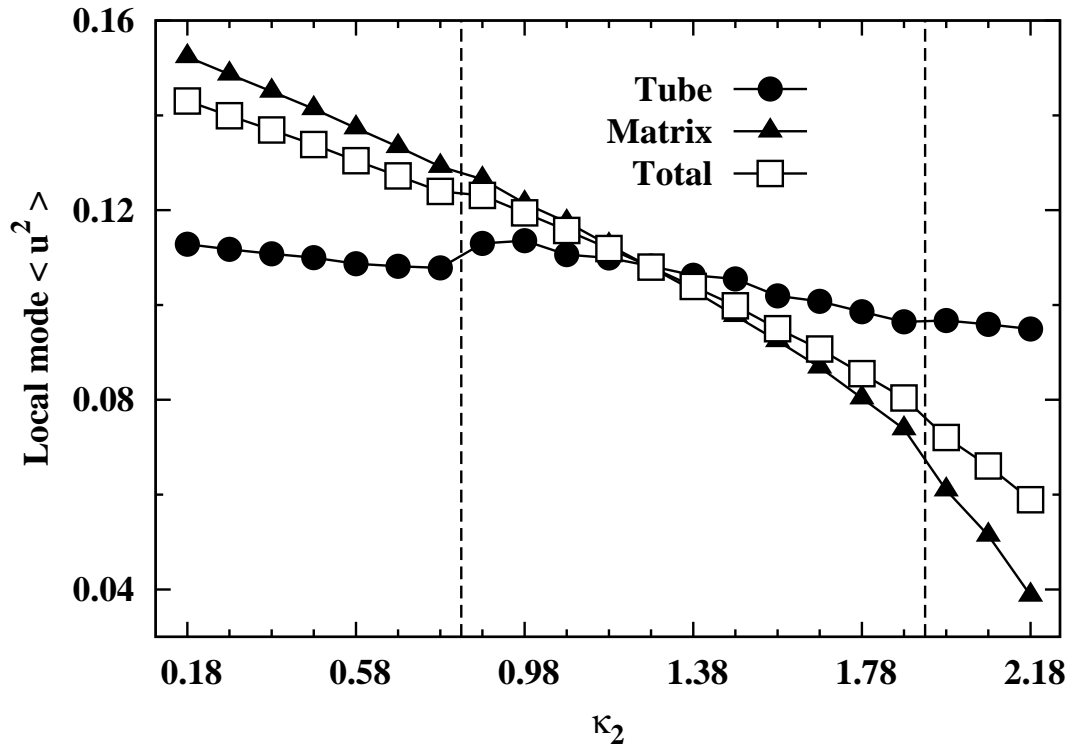
Figure 3.3: Average $< u^2 >$ of the individual dipoles inside the tube (symbols of dots) and in the matrix (symbols of triangles) at 64 K. The average $< u^2 >$ of all dipoles in the whole system is also shown (in squares) for comparison.

3.3.2 Microscopic insights of structural phases

To reveal the reasons that cause the different polarization behaviors in Fig.3.2, we now provide microscopic insights which, we hope, will be useful for understanding the three structural phases. Fig.3.4 presents the dipole patterns on different cross-section planes for various κ_2. At κ_2=1.88 (which is the largest κ_2 that yields phase I), Fig.3.4a shows that dipoles in the matrix are rather uniformly pointing at x, but dipoles in the tube deviate from the x direction in a subtle way. In fact, the upper half dipoles in the tube rotate clockwise, while the lower half dipoles rotate anticlockwise. As a consequence, an interesting dipole pattern of two "half-vortices" is formed inside the tube. These half vortices, as will become clear later, play an important role in terms of understanding the structural properties in FE tube array. Fig.3.4a reveals that FE half vortex can be nucleated directly out of ordinary polarization in ferroelectric materials. Formation of FE half vortex is far less common than FE polarization or FE vortex, and can be intuitively understood as follows. At κ_2=1.88, the polarization magnitude in the matrix ($P \sim 0.4 \text{C/m}^2$) is smaller than that in the PZT tube ($P \sim 0.75 \text{C/m}^2$). Dipoles inside the tube must rotate in order to satisfy the electrical boundary conditions, leading to the dipole pattern in Fig.3.4a. Also note in Fig.3.4a that, despite the formation of two half-vortices, the macroscopic total polarization remains large and predominantly points at the x direction, which explains why the whole system behaves like a ferroelectric phase.

When κ_2 is increased to 1.98 (which is the initial stage of phase II), Fig.3.4b shows that dipoles form a complex Ω-shaped structure. More specifically, dipoles in the upper half vortex remain to rotate clockwise as in Fig.3.4a, but a majority of dipoles in the lower half vortex flip their directions and rotate also into clockwise, forming a configuration as in Fig.3.4b. Note in Fig.3.4b that a significant number of dipoles in the tube are no longer pointing along x axis, which is responsible for the sharp decline of the P_x polarization of phase II in Fig.3.2.

The physics behind the formation of the Ω-shaped dipole structure (Fig.3.4b) is non-

trivial. Let us begin with Fig.3.4a. In Fig.3.4a, regions A and B (i.e., where the two half vortices meet) are special and act as two topological defects. Near these two regions, dipoles inside and outside the tube both point along x. However, since dipoles in the matrix have a smaller magnitude (due to larger κ_2) than the ones inside the tube, dipoles in region A (or B) need to rotate toward the z axis as required by boundary condition, which is indeed confirmed by our calculated dipole pattern on the xz cross section (not shown). This dipole rotation toward z-axis increases the strain energy of regions A and B, since other dipoles in
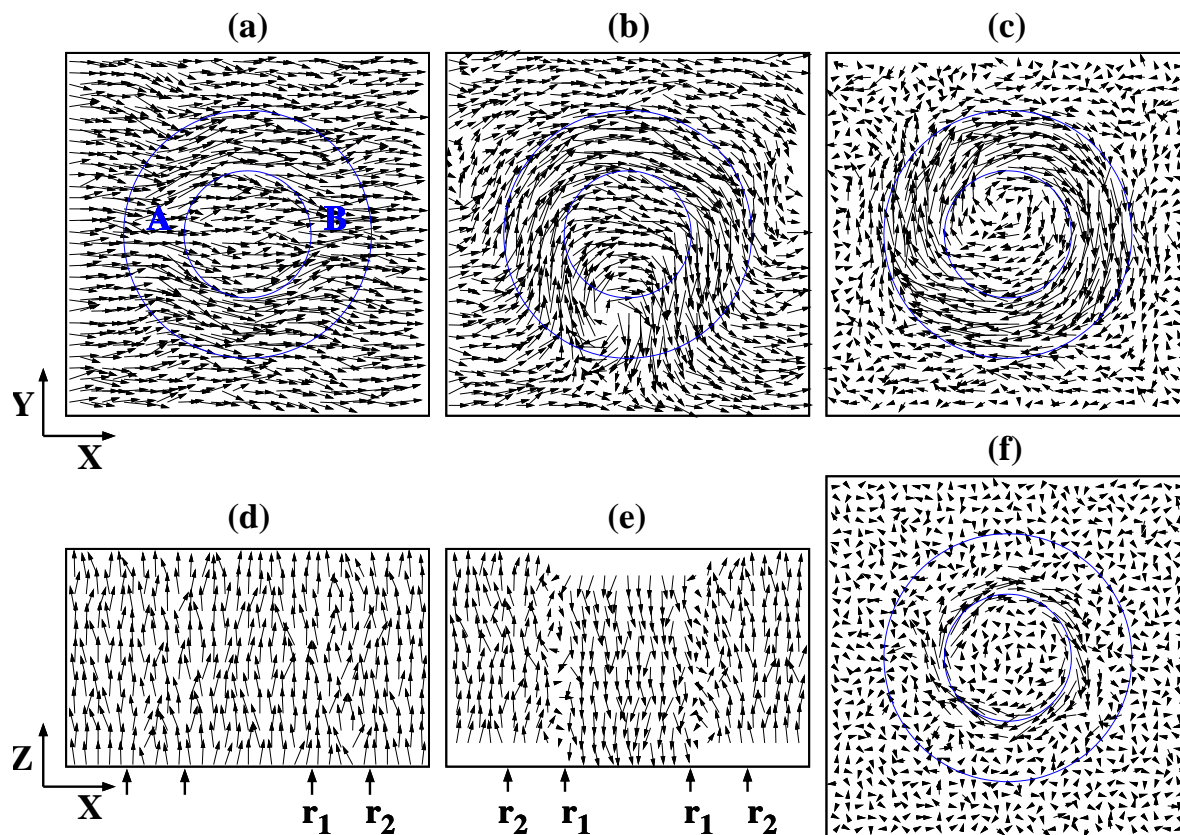
Figure 3.4: Microscopic dipole patterns at 64 K on the following cross-section planes and at the following κ_2: (a) on the central xy plane for $\kappa_2 = 1.88$; (b) on the central xy plane for $\kappa_2 = 1.98$; (c) on the central xy plane for $\kappa_2 = 2.18$; (d) on the central xz plane for $\kappa_2 = 0.88$; (e) on the central xz plane for $\kappa_2 = 0.78$; (f) on the central xy plane for $\kappa_2 = 0.78$. The boundary of the PZT tube is indicated by two thin concentric circles on the central xy plane in (a)-(c) and (f), and by the thick arrows at the bottom of figure in (d) and (e).

the tube rotate within the xy plane while dipoles in regions A and B rotate out of the xy plane. As κ_2 is increased to 1.98 in Fig.3.4b, the strain energy caused by the z-axis dipole rotation in regions A and B is too high; as a result, the dipoles in these two regions cease to rotate toward the z direction. Instead, they rotate also clockwise within the xy plane to comply with the upper half vortex, giving rise to the Ω-shaped structure in Fig.3.4b.

When κ_2 is further increased to 2.18 (Fig.3.4c), dipoles inside the tube all rotate clockwise and form a vortex. The formation of FE vortex explains why **P** vanishes along all three directions at $\kappa_2 = 2.18$ in Fig.3.2. The evolution from Fig.3.4a to Fig.3.4c reveals that FE vortex in tube array is nucleated from half vortices, and the Ω-shaped dipole structure serves as a bridge connecting the ferroelectric phase (Fig.3.4a) and the vortex phase (Fig.3.4c).

FE vortex is not new and was reported before[13]. However, unlike FE vortex in nanodots,[13] vortex in Fig.3.4c is caused by completely different mechanism. Vortex in nanodots is caused by strong depolarization field along all three directions,[13] which forces dipoles to adopt a vortex structure. In contrast, vortex in Fig.3.4c is caused by long range tube-tube interaction. To prove the latter, we have performed calculations for a single PZT tube without tube-tube interaction, and we found a ferroelectric phase with polarization along the tube axis as it should be (since there is no depolarization field along the tube axis). The polarization phase predicted in a single tube is also consistent with the experimental measurement that a ferroelectric hysteresis loop was observed in a single tube[19]. However, when tube-tube interaction is included by forming a FE tube array, a vortex phase as in Fig.3.4c becomes more stable. These calculations thus demonstrate that the vortex in Fig.3.4c is indeed caused by tube-tube interaction. Furthermore, unlike a single vortex in FE nanodot[13], the vortices in FE tube array form a *vortex array*, which is more interesting since the vortex array allows us to switch one or several vortices (by, for instance, curled electric fields[42]) and then study how other vortices respond (which will lead to important knowledge on vortex-vortex interaction).

To understand phase III, we compare the dipole pattern on the central xz plane at

κ_2=0.88 (which belongs to phase I, Fig.3.4d) with that at κ_2=0.78 (which belongs to phase III, Fig.3.4e). Dipoles in Fig.3.4d are fairly uniform and point at $+z$, forming a P_z *monodomain*. This is consistent with the P_z ferroelectric phase in Fig.3.2. In sharp contrast, at κ_2=0.78 in Fig.3.4e, dipoles form a stripe-like *multidomain* since dipoles inside the inner radius r_1 (i.e., $r < r_1$) point at $-z$ while dipoles outside r_2 point at $+z$. Due to formation of the $-z$ domain, the total polarization in Fig.3.4e is considerably smaller than in Fig.3.4d, explaining the sudden decrease of polarization at the boundary between phase I and phase III in Fig.3.2. More intriguingly, Fig.3.4e shows that inside the wall between two opposite domains (i.e., in the region between r_1 and r_2 in Fig.3.4e), P_z displays an evident polarization gradient, namely P_z near r_1 is small while P_z near r_2 is very large. The P_z gradient inside the domain wall poses another interesting question concerning what happen to the dipoles in the *tube* while dipoles in the *matrix* form a multi-domain. To answer this question we plot in Fig.3.4f the dipole pattern on the central xy plane at the same κ_2 as in Fig.3.4e, showing that dipoles inside the tube simultaneously develop a vortex near r_1 (i.e., at the location where P_z is small). The microscopic insight thus shows that phase III is very unusual in the sense that a FE stripe domain (which is a linear polarization) and a FE vortex (which is a circular polarization) coexist in the same system. To the best of our knowledge, this is the first example of such a structural phase in ferroelectric systems.

FE stripe domains have already attracted a lot of interesting attentions.[7, 8] Structural phases with coexisting stripe domain and FE vortex are more intriguing in the sense that these structures allow us to probe the stripe-vortex interaction by, e.g., applying electric field to vary the stripe domain and then studying how the vortex respond. Meanwhile, it is useful to point out that the stripe domain in Fig.3.4e is caused by different mechanism than the stripe domain previously discovered in FE films[7, 8, 9]. Stripe domain in FE films is formed in order to reduce the out-of-plane depolarization field.[7, 8, 9] However, the stripe domain in Fig.3.4e is not caused by the depolarization field since this field is zero along the z-axis. Instead, the stripe domain in Fig.3.4e is formed because it lowers the long-range Coulomb

energy among dipoles in the matrix.

3.3.3   High-temperature structural phases

In Sec.3.3.1 and 3.3.2, structural phases at a low temperature of 64K were reported. We now examine the structural phases at high temperatures, since ferroelectric ordering is often sensitive to thermal excitation. Fig.3.5a depicts the net polarization P_x and net toroid moment G_z at different temperatures for the κ_2=1.68 case. The other components of polarization (i.e., P_y and P_z) and the other components of toroid moment (i.e., G_x and G_y) are all negligible at any temperatures. Toroid moment is defined as $\mathbf{G} = \frac{1}{N} \sum_i \mathbf{r}_i \times \mathbf{d}_i$, where $\mathbf{r}_i$ and $\mathbf{d}_i$ are the position and local dipole moment at site i, respectively.

Three main conclusions can be drawn from Fig.3.5a: (i) At low temperatures T <360K, P_x is large and the structure is clearly a ferroelectric phase, consistent with Fig.3.2. (ii) However, FE phase is not stable at temperatures $360 < T < 630$ K, during which P_x vanishes. Interestingly, toroid moment G_z is large in this temperature range, showing that the system is a vortex phase. The onset of the G_z vortex phase occurs at ~630K. (iii) At T=360K, the system undergoes a sharp phase transition from the G_z vortex phase to the P_x polarization phase. Conclusion (iii) is particularly interesting since it demonstrates that a vortex phase can *spontaneously* transform into a polarization phase by temperature alone, despite the fact that these two structural phases have entirely different order parameters. We should point out that the spontaneous vortex/polarization phase transition in Fig.3.5a is in profound difference from the transition in Ref.[43] where external uniform electric field was applied to transform FE vortex into polarization; therefore the latter is not a spontaneous phase transition.

The origin for the spontaneous vortex/polarization phase transformation in Fig.3.5a can be attributed to the interaction between tube and matrix, thereby the existence of the matrix is important. When temperature is between 360 and 630 K, dipoles in the PZT tube develop an ordered vortex phase first, while dipoles in the matrix are random and relatively

small in magnitude due to large κ_2. When temperature is decreased below 360 K, dipoles in the matrix begin to order. However, dipoles in the matrix do not like to order in the
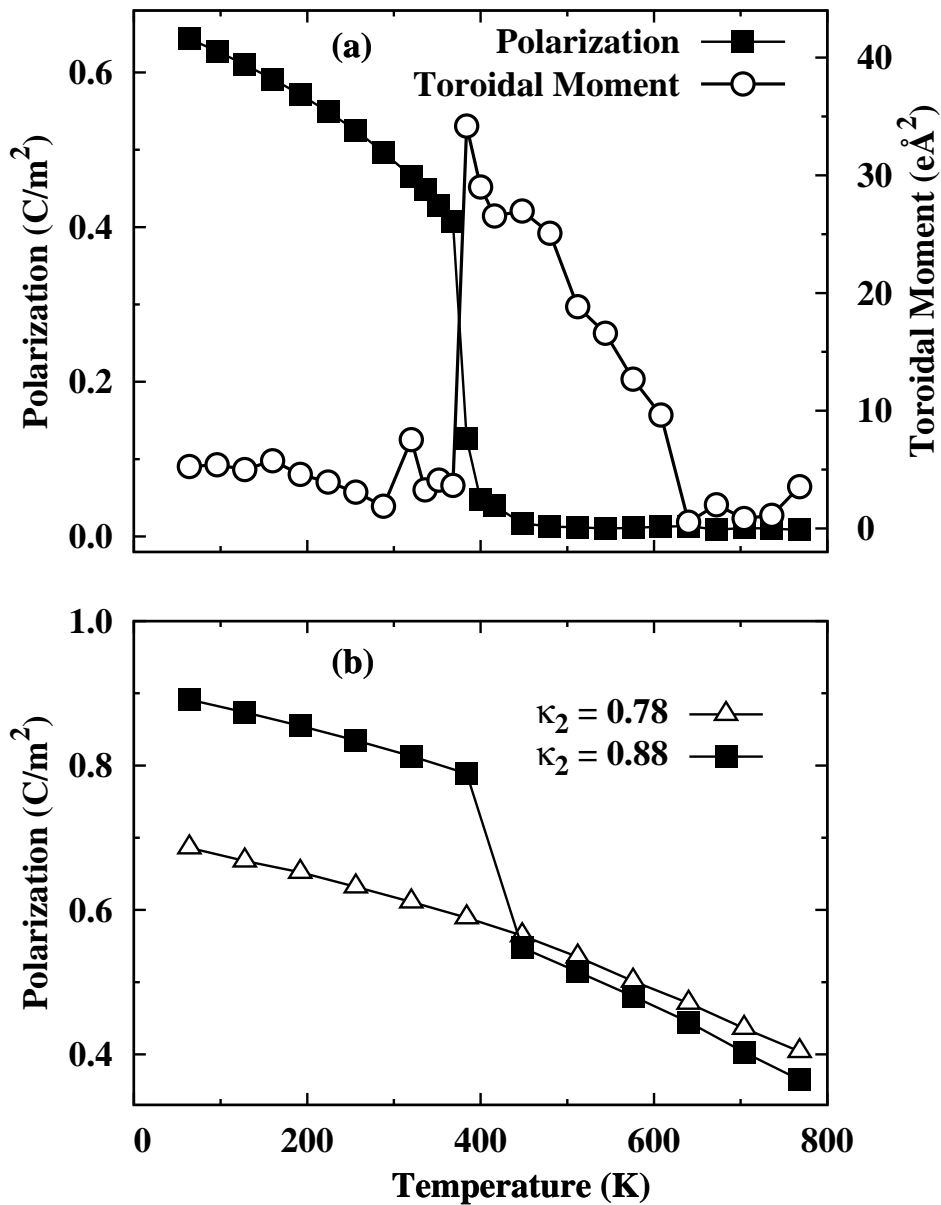
Figure 3.5: (a) Polarization P_x (using the left vertical axis) and toroidal moment G_z (using the right axis) as a function of temperature for $\kappa_2 = 1.68$. (b) Net P_z polarization as a function of temperature for $\kappa_2 = 0.88$ and $\kappa_2 = 0.78$.

same way as those in the tube (namely forming a vortex), since the circular-like vortex phase will significantly increase the strain energy near the boundary of supercell. Instead a ferroelectric polarization phase is preferred in the matrix, and consequently forces dipoles in the tube to transform also into the polarization phase, which causes the spontaneous vortex/polarization phase transformation. By using statistical correlation method[37], we find that the vortex/polarization transition at 360K yields a large dielectric response of $\chi_{33} \approx 7000$ and an electromechanical response of $d_{33} \approx 200$ pC/N.

We have performed calculations at high temperatures for other κ_2. Our calculations show that the phase sequence in Fig.3.5a—namely, a cubic phase at high temperatures, a vortex phase at intermediate temperatures, and then a ferroelectric phase at low temperatures—persists when κ_2 is in the range $1.48 \leq \kappa_2 \leq 2.08$. On the other hand, when $\kappa_2 \geq 2.18$, the vortex phase is stable to very low temperatures without transformation into the polarization phase. This is because the magnitudes of dipoles in the matrix are too small when κ_2 is above 2.18, and the interaction between the matrix and the tube is not sufficient to cause the phase transformation. The lack of vortex/polarization transition for $\kappa_2 \geq 2.18$ further supports the conclusion that the interaction between tube and matrix is responsible for the transition.

To reveal the high-temperature phases when $\kappa_2 < 1.48$, we depict in Fig.3.5b the P_z polarizations at different temperatures for κ_2=0.88 and κ_2=0.78. Recall that, at a low temperature of 64K, κ_2=0.88 yields phase I while κ_2=0.78 leads to phase III (Fig.3.2). Now at *high* temperatures, the κ_2=0.78 curve in Fig.3.5b shows that P_z varies smoothly with temperature, implying that the multi-domain structure of phase III does not undergo any drastic change during the temperature annealing, or in other words, the multi-domain structure of phase III starts at high temperatures and proceeds to very low temperatures. However, this is not the case for the κ_2=0.88 curve in Fig.3.5b, where two interesting observations can be made: (i) At high temperatures its P_z is close to that of κ_2=0.78, showing that both systems have stripe multi-domain; (ii) When temperature is annealed to $\sim$400K, P_z of κ_2=0.88

suddenly jumps. By examining the dipole patterns, we find that the sudden P_z jump for κ_2=0.88 is caused by the fact that the dipoles pointing at $-z$ in the stripe domain (see, e.g., Fig.3.4e) flip into the $+z$ direction and form a single domain, which explains why P_z at $T <$400 K in Fig.3.5b is larger for κ_2=0.88 than for κ_2=0.78. We thus obtain from Fig.3.5b that, when $\kappa_2 <$1.48, stripe domains develop at high temperatures for both phases I and III. As temperature is annealed, stripe domain flips and becomes a single ferroelectric domain for phase I. But for phase III, the stripe domain persists to low temperatures.

3.4 Summary

We have determined finite-temperature structural and polarization properties of PZT tube array embedded in matrix medium of different ferroelectric strengths. A range of matrix media were considered, including strongly FE, moderately FE, weakly FE, incipient-like paraelectric, and strongly paraelectric. The FE properties of the tube array were found to be strongly influenced by the matrix, revealing a rich variety of structural phases. Beyond describing structural phases using order parameters such as polarization and toroid moment (which are good in terms of describing collective behaviors on the macroscopic level), we further identified and provided microscopic insights for understanding individual structural phases. These microscopic insights may be difficult to obtain in experiments and/or in small scale first-principles calculations. The study revealed how one structural phase evolves into another and how a new structural phase is nucleated in PZT tube array. Moreover, we showed that high-temperature structural phases in PZT tube array could be interestingly different from the low-temperature phases. Some of our specific findings are summarized in the following.

(i) Macroscopic polarization in PZT tube array can be drastically changed by matrix. (ii) Depending on matrix, the PZT tube array may behave 3D-like (phase I in which polarization may point at any of the x, y, or z direction), or 2D-like (phase II in which polarization prefers either x or y, but not z, direction), or 1D-like (phase III in which polarization prefers only z). (iii) Two structural phases that do not exist in bulk PZT are predicted in PZT tube array. One is the vortex phase when matrix is paraelectric (e.g., at $\kappa_2 \geq 2.18$). Differing from FE vortex in nanodots which is caused by depolarization field, the vortex phase in PZT tube array originates from long range tube-tube interaction. Phase III is another structural phase that does not exist in bulk PZT. Phase III is unusual in the sense that it is formed by the coexistence of 180-degree stripe domain and FE vortex, where the vortex is formed within the domain wall.

(iv) Our simulations reveal that the nucleation of FE vortex in tube array begins with

two half-vortices. (v) Regions A and B, where the two half vortices meet, act as topological defects, by which the half-vortices evolve into a peculiar Ω-shaped structure. This Ω-shaped structure serves as a key bridge connecting phase I and phase II. (vi) We further showed that a vortex phase can spontaneously transform into a polarization phase by varying the temperature alone, without need of external electric fields, despite that the considered two phases have entirely different order parameters. The tube-matrix interaction is found to be responsible for this uncommon spontaneous phase transition. (vii) The tetragonal phases in bulk $Pb(Zr_{0.5}Ti_{0.5})O_3$ and in PZT tube array have distinct phase formation paths, manifesting the different interactions in two systems. The tetragonal phase in bulk $Pb(Zr_{0.5}Ti_{0.5})O_3$ evolves from a cubic phase when temperature is lowered, but the tetragonal phase in PZT tube array evolves from a vortex phase when $1.48 \leq \kappa_2 \leq 1.88$. (viii) For phase III, the FE stripe domain starts at high temperatures and proceeds to low temperatures without domain flipping. However, for $\kappa_2 = 0.88$ (which belongs to phase I), the stripe domain flips to form a single domain at low temperatures. Since phase transition and structure formation in systems of reduced dimension is a topic of profound interest for decades, we hope that the unusual properties found here in FE nanotube array will stimulate further theoretical and experimental interests in this novel form of FE nanostructures.

Bibliography

[1] M. Dawber, K.M. Rabe, and J.F. Scott, Rev. Mod. Phys. **77**, 1083 (2005).

[2] D.G. Schlom, L.-Q. Chen, C.-B. Eom, K.M. Rabe, S.K. Streiffer, and J.-M. Triscone, Ann. Rev. Mater. Res. **37**, 589 (2007).

[3] H. N. Lee, H. M. Christen, M. F. Chisholm, C. M. Rouleau, and D. H. Lowndes, Nature (London) **433**, 395 (2005).

[4] J.B. Neaton and K.M. Rabe, Appl. Phys. Lett. **82**, 1586 (2003).

[5] N. Sai, B. Meyer, and D. Vanderbilt, Phys. Rev. Lett. **84**, 5636 (2000).

[6] J. Junquera and P. Ghosez, Nature (London) **422**, 506 (2003).

[7] S. K. Streiffer, J.A. Eastman, D.D. Fong, C. Thompson, A. Munkholm, M.V. Ramana Murty, O. Auciello, G.R. Bai, and G.B. Stephenson, Phys. Rev. Lett. **89**, 067601 (2002).

[8] I. Kornev, H. Fu, and L. Bellaiche, Phys. Rev. Lett. **93**, 196104 (2004).

[9] P. Aguado-Puente and J. Junquera Phys. Rev. Lett. **100**, 177601 (2008).

[10] D.D. Fong, G.B. Stephenson, S.K. Streiffer, J.A. Eastman, O. Auciello, P.H. Fuoss and C. Thompson, Science **304**, 1650 (2004).

[11] C. Liu, B. Zou, A. J. Rondinone, and Z. J. Zhang, J. Am. Chem. Soc. **123**, 4344 (2001).

[12] A. O'Brien, L. Brus, and C. B. Murray, J. Am. Chem. Soc. **123**, 12085 (2001).

[13] I. I. Naumov, L. Bellaiche, and H. Fu, Nature (London), **432**, 737 (2004).

[14] W.S. Yun, J. J. Urban, Q. Gu, and H. Park, Nano. Lett. **2**, 447 (2002).

[15] Z. Wang, J. Hu, and M.-F. Yu, Appl. Phys. Lett. **89**, 263119 (2006).

[16] I. I. Naumov and H. Fu, Phys. Rev. Lett. **95**, 247602 (2005).

[17] G. Geneste, E. Bousquet, J. Junquera, and P. Ghosez, Appl. Phys. Lett. **88**, 112906 (2006).

[18] J. Hong, G. Catalan, D. N. Fang, E. Artacho, and J. F. Scott, Phys. Rev. B **81**, 172101 (2010).

[19] Y. Luo, I. Szafraniak, and N. D. Zakharov, V. Nagarajan, M. Steinhart, R.B. Wehrspohn, J.H. Wendorff, R. Ramesh, M. Alexe, Appl. Phys. Lett. **83**, 440 (2003).

[20] F.D. Morrison, Y. Luo, I. Szafraniak, V. Nagarajan, R.B. Wehrspohn, M. Steinhart, J.H. Wendorff, N.D. Zakharov, E.D. Mishina, K.A. Vorotilov, A.S. Sigov, S. Nakabayashi, M. Alexe, R. Ramesh, and J.F. Scott, Rev. Adv. Mater. Sci. **4**, 114 (2003).

[21] S. Iijima, Nature (London) **354**, 56 (1991).

[22] N. G. Chopra, R. J. Luyken, K. Cherrey, V. H. Crespi, M. L. Cohen, S. G. Louie, and A. Zettl, Science 269, 966 (1995).

[23] M.E. Lines and A.M. Glass, *Principles and Applications of Ferroelectrics and Related Materials* (Clarendon, Oxford, 1979).

[24] O. Auciello, J.F. Scott, and R. Ramesh, Phys. Today **51**, 22 (1998).

[25] K. Uchino, *Piezoelectric Actuators and Ultrasonic Motors* (Kluwer Academic, Boston, 1996).

[26] J.F. Scott, *Ferroelectric Memories* (Springer, Berlin, 2000).

[27] S. Prosandeev and L. Bellaiche, Phys. Rev. Lett. **97**, 167601 (2006).

[28] L.D. Landau and E.M. Lifshitz, *Statisical Physics, Part 1* (Pergamon, NY, 1980).

[29] N. D. Mermin and H. Wagner, Phys. Rev. Lett. **17**, 1133 (1966).

[30] P. Bruno, Phys. Rev. Lett. **87,** 137203 (2001).

[31] R. E. Cohen, Nature (London) **358**, 136 (1992).

[32] R. E. Cohen and H. Krakauer, Phys. Rev. B **42**, 6416 (1990).

[33] B. Noheda, D. E. Cox, G. Shirane, R. Guo, B. Jones, and L. E. Cross, Phys. Rev. B **63**, 014103 (2000).

[34] W. Zhong, D. Vanderbilt, and K.M. Rabe, Phys. Rev. Lett. **73**, 1861 (1994).

[35] L. Bellaiche, A. Garcia, and D. Vanderbilt, Phys. Rev. Lett. **84**, 5427 (2000).

[36] L. Bellaiche, A. Garcia, and D. Vanderbilt, Ferroelectrics **266,** 41 (2002).

[37] A. Garcia and D. Vanderbilt, Appl. Phys. Lett. **72**, 2981 (1998).

[38] J. Iniguez and D. Vanderbilt, Phys. Rev. Lett. **89**, 115503 (2002).

[39] I. I. Naumov and H. Fu, cond-mat/0505497 (2005).

[40] P. Zubko, G. Catalan, A. Buckley, P.R.L. Welche, and J. F. Scott, Phys. Rev. Lett. **99**, 167601 (2007).

[41] U. Chon, H. M. Jang, M. G. Kim, and C. H. Chang, Phys. Rev. Lett. **89**, 087601 (2002).

[42] I. I. Naumov and H. Fu, Phys. Rev. Lett. **101**, 197601 (2008).

[43] I. I. Naumov and H. Fu, Phys. Rev. Lett. **98**, 077603 (2007).

Chapter 4

LaO δ-doped SrTiO$_3$

4.1   Introduction

Oxide electronics starts to attract intense attention recently, driven by the fact that oxides offer a rich variety of interesting properties such as ferroelectricity, ferromagnetism, colossal magnetoresistance, transparent conductivity, superconductivity, etc[1, 2]. These properties are often hard to come by in traditional semiconductors of microelectronics. The oxide electronics was further motivated by the discovery of a surprising electrical conductivity at the interface of two insulating oxides LaAlO$_3$ and SrTiO$_3$,[3] which also displays weak ferromagnetism[4] and superconductivity[5] at very low temperatures. Since these experimental discoveries, many theoretical studies have been devoted to this and similar systems, yielding important understanding on the electronic structure[6, 7, 8, 9], lattice-screening effect[10, 11], metal-induced gap state[12], electrical properties[13], and the effects of vacancies[14]. The conductivity and/or superconductivity in LaAlO$_3$/SrTiO$_3$ have been utilized in the application of field transistors[15, 16]. In addition to the LaAlO$_3$/SrTiO$_3$ system, another example in pursuing oxide electronics is the recent finding of conductivity at SrTiO$_3$ surface[17].

In microelectronics, δ-doping has become an important approach in designing electronic structures. It was successfully used in semiconductor electronics to create two-dimensional electron gas (2DEG). Nowadays, the advance of molecular beam epitaxy (MBE) technique has enabled δ-doping also in perovskite oxides[2, 18]. Indeed, δ-doping of a single LaO atomic layer in n bulk-cells of SrTiO$_3$ has been experimentally demonstrated,[19] where the supercell periodicity n can be varied. Furthermore, interesting transport properties were observed in this δ-doped SrTiO$_3$. Pure SrTiO$_3$ itself is a insulator. However, after δ-doping

of a LaO layer, two different channels of conductivity were found in the measurement of the magnetic-field dependence of the Hall resistivity, one with high electron mobility and the other with considerably lower electron mobility[19]. The high-mobility conductivity in δ-doped perovskites offers another promising avenue for oxide electronics. This is one of the reasons that we are interested in LaO δ-doped $SrTiO_3$ in this study. While the measurement result that LaO-doped $SrTiO_3$ conducts is important, it is nevertheless not clear in terms of (i) how many conduction bands are below the Fermi energy, (ii) what are the microscopic states of those conducting bands, and (iii) to what extent one can modify those conducting electrons.

Modification of properties in a given solid, in order to reveal different physics as well as to suit different purposes of technological applications, has been one of the most utilized approaches in achieving better understanding of physics. One effective method to modify the electronic properties of δ-doped $SrTiO_3$ is by inplane biaxial strain. Unlike hydrostatic pressure, inplane strain changes interatomic interactions and chemical bonds differently along the out-of-plane direction (as compared to the inplane direction), creating an anisotropic way of tuning the electronic properties. With respect to undoped cubic $SrTiO_3$, two mechanisms simultaneously alter the electronic structure in LaO-doped $SrTiO_3$ under inplane strain: one is atomic-scale δ doping and the other is the homogeneous inplane strain. Interplay of these two mechanisms makes the electronic structure interesting and difficult to predict, which explains why we are interested in studying the inplane-strain effects in δ-doped $SrTiO_3$.

Furthermore, bulk $SrTiO_3$ is known to display ferroelectric off-center displacements along the out-of-plane direction when the compressive inplane η strain is above a certain critical value η_c[20, 21]. In LaO-doped $SrTiO_3$, δ-doping shall cause a redistribution of ionic and electronic charges and hence a change of the screening effect with respect to bulk $SrTiO_3$. It is thus of interest to study what is the critical inplane strain that may cause the δ-doped $SrTiO_3$ to develop the out-of-plane off-center displacements, or whether such off-center displacements exist at all. Obviously the off-center displacements, even if they exist, are not expected to

cause ferroelectricity in LaO-doped $SrTiO_3$ because electrons in a metallic system will screen the ferroelectricity. But appearance of these off-center displacements will nevertheless further alter the electronic states. This makes the study of the electronic structures in LaO δ-doped $SrTiO_3$ even more complex if the off-center displacements do emerge. Driven by these potentially rich phenomena to be caused by the interplay of δ-doping, inplane strain, and off-center displacements, a study is thus needed to determine the influence of inplane strain on the electronic structure of LaO-doped $SrTiO_3$.

In this work, we perform first-principles density functional calculations to reveal the effects of inplane strain in LaO δ-doped $SrTiO_3$. We study both the structural properties (from which one can determine off-center displacements) and electronic properties (from which one may infer what electron states are responsible for the conductivity and how they are affected by the imposed strain). Various quantities including cation-anion displacements, electron potentials, band structure, wave function localizations, and electron velocity are calculated. Our calculations show that strain can cause interesting (and sometimes drastic) changes to these physical properties. The results not only are useful to explain the experimental observations, but also yield microscopic understanding of the electronic states in δ-doped $SrTiO_3$. The paper is organized as follows. The technique details of the theoretical method are described in Sec.4.2. We then present in Sec.4.3.1 the electronic structures in δ-doped $SrTiO_3$ under different inplane strains. The structural properties caused by inplane strains are given in Sec.4.3.2, including the electron potential which serves as a connection bridging the structural properties and electronic properties. Finally, conclusions are summarized in Sec.4.4.

4.2 Theoretical methods

We consider the LaO-doped $SrTiO_3$ as shown schematically in Fig.4.1, where eight perovskite bulk cells of 40 atoms are stacked along the z-axis which consist of alternating SrO and TiO_2 planes. δ-doping is mimicked by replacing one SrO layer by LaO. The supercell in Fig.4.1 is repeated along the z-axis. We choose to consider a supercell of eight bulk cells because a similar structure was fabricated in experiment[19], where δ-doped superlattices of either six bulk cells or ten bulk cells were grown. Inplane compressive strain, $\eta = \frac{|a-a_0|}{a_0}$, is imposed on the xy plane with respect to the equilibrium inplane lattice constant a_0 of bulk $SrTiO_3$. Different inplane η strains are considered. The ratio c/a for the supercell is determined to be 8.49, 8.76, and 9.24 for $\eta =3\%$, 4%, and 5%, respectively. For each cell structure, atomic positions are fully relaxed.

Technically we use first-principles density functional calculations within local-density approximation (LDA) to determine total energy and atomic forces, as implemented in Quantum Espresso[22, 23]. Norm-conserving pseudopotentials are used[24], and semicore states Ti $3s$ and $3p$ are treated as valence states. The energy cutoff for the plane-wave expansion of wave functions is 80 Ry, which is checked to be sufficient. The Sr, Ti, O pseudopotentials have been previously used to study structural, phonon, and polarization structure in $SrTiO_3$,[25] giving a lattice constant of 3.86Å for cubic $SrTiO_3$ which is consistent with other theoretical calculations. To test our pseudopotentials for La and Al, we apply them to bulk cubic $LaAlO_3$, yielding a lattice constant of 3.75 Å and a bulk modulus of 223 GPa, which agree with 3.752 Å and 217 GPa in another calculation[26].

An open question concerns whether one should use LDA or LDA+U to perform the structure optimization for LaO-doped $SrTiO_3$. As pointed by Hamann *et al.*, although bulk $LaTiO_3$ is considered to be a Mott insulator with strong correlation, a single LaO layer is not[10]. Here we give another reason that LDA rather than LDA+U is preferred, namely we found that the latter yields incorrect atomic structures and ferroelectric off-center displacements for strained and undoped bulk $SrTiO_3$ (with 5 atoms a cell), as demonstrated

in Fig.4.2. When a compressive strain exceeds the critical value of $\sim 1\%$, bulk $SrTiO_3$ is known to develop a Ti-O off-center displacement and a polarization[20, 21]. In Fig.4.2, a inplane strain of 3% (larger than the critical value) is applied to bulk $SrTiO_3$; both LDA and LDA+U are used to determine the total energy and Ti-O displacement as a function of c/a. For each c/a, the internal atomic positions are fully relaxed. We see from the total energy in Fig.4.2 that LDA and LDA+U yield similar optimal $c/a = 1.06$. At this optimal c/a, LDA gives a large Ti-O displacement and thus a large polarization (see the symbols of solid dots). However, the Ti-O displacement obtained from LDA+U remains null at $c/a = 1.06$ (see the symbols of empty dots). The LDA+U result is not consistent with experiments[27] and/or
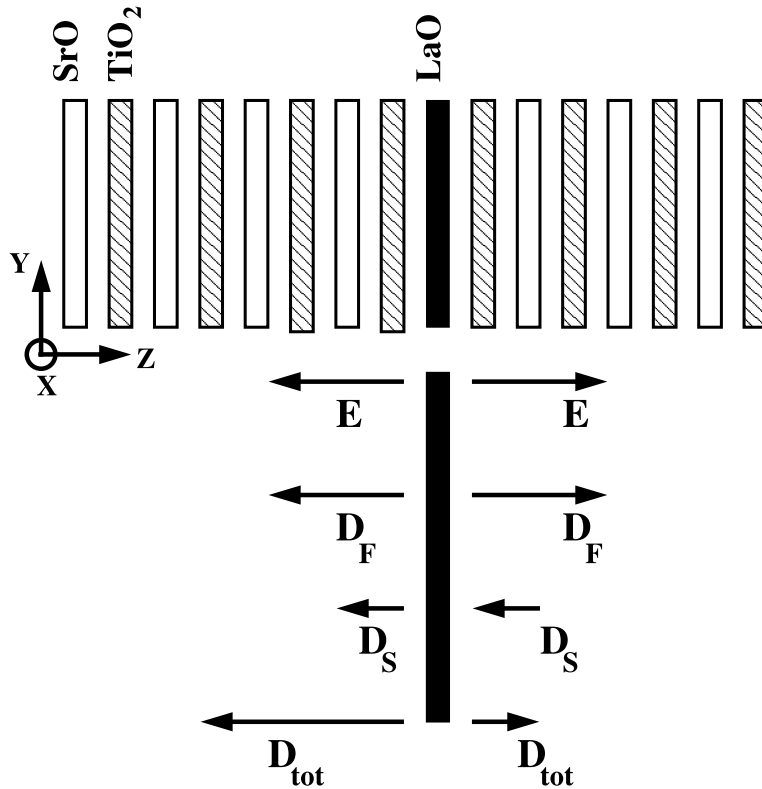
Figure 4.1: A schematic illustration of the supercell and the LaO doping layer. The z-axis is along the crystalographic [001] direction. Inplane strain is on the xy plane. In the lower part of the figure, the electric field $\mathbf{E}$ generated by the LaO layer, the field-induced cation-anion displacement $\mathbf{D}_F$, the strain-induced displacement $\mathbf{D}_S$, and the total displacement $\mathbf{D}_{tot} = \mathbf{D}_F + \mathbf{D}_S$ are shown schematically.

LDA calculations[20, 21]. We thus decide to use LDA to perform structure optimization.

After the structural optimization, the well-known LDA gap problem arises when we study band structure. Ideally one wishes to perform GW theory or hybrid density functional calculations, which is computationally intensive for large supercells. Here we use a computationally less demanding but tractable approach, by determining band structure (not optimal
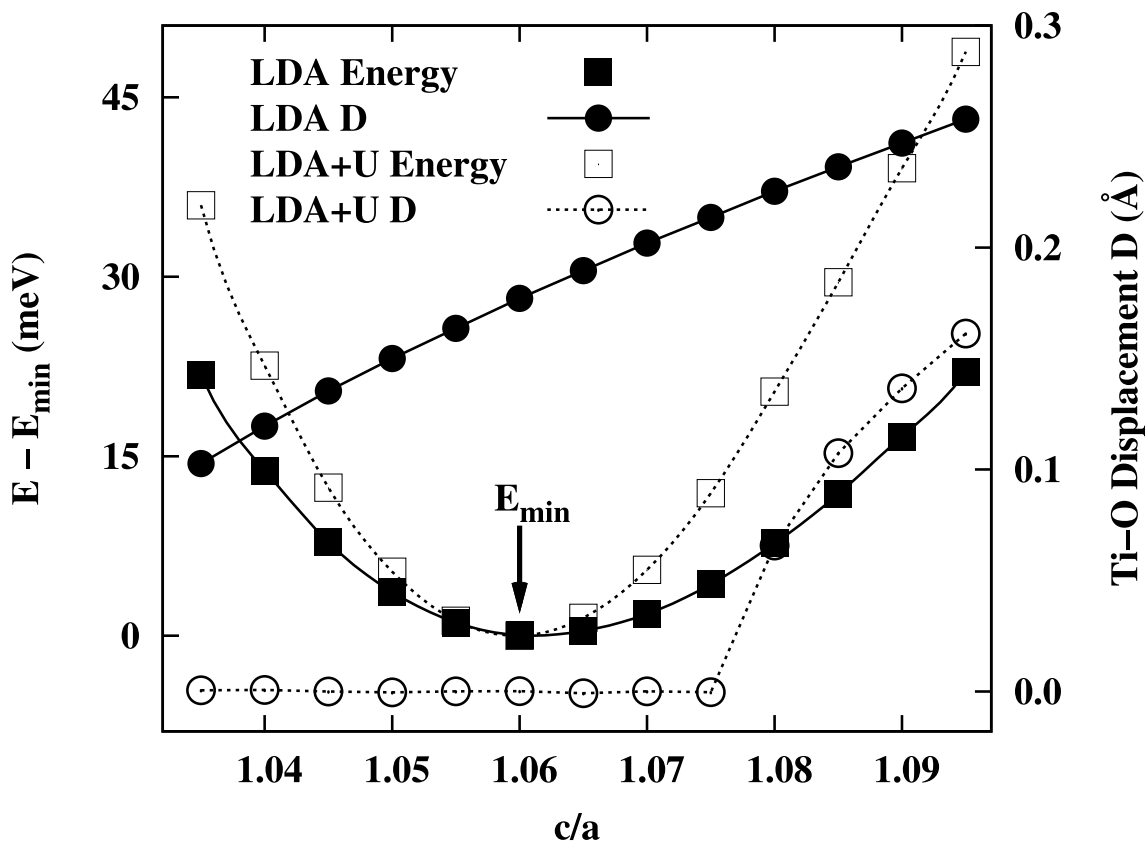
Figure 4.2: Calculated total energies (solid and empty squares, using the left vertical axis) and Ti-O displacements (solid and empty dots, using the right vertical axis) as a function of c/a in bulk $SrTiO_3$ under a 3% compressive inplane strain. For total energies, solid squares are obtained from LDA calculations while empty squares are obtained from LDA+U calculations. The lowest energy at optimal c/a, E_{min}, is used as the zero energy reference for both LDA and LDA+U calculations. For Ti-O displacements, solid dots are obtained from LDA calculations while empty dots are obtained from LDA+U calculations.

atomic geometry) using LDA+U calculations which partially alleviate the LDA band-gap problem. Similar approach of using LDA+U to correct band gap has been used in other calculations[28, 29, 30]. We use $U = 8.5$eV for La, yielding a band gap of 5.48 eV for LaAlO$_3$, as compared to a LDA band gap of 3.27 eV. The experimental band gap of LaAlO$_3$ is 5.50 eV[31]. We use $U = 6.0$eV for Ti, which gives a direct band gap of 3.07 eV at Γ and an indirect band gap of 2.63 eV between CBM at Γ and VBM at R. These values are better than the LDA gaps of 2.16 eV (direct) and 1.82 eV (indirect), respectively. But the direct band gap of LDA+U (3.07 eV) is still slightly below the corresponding one obtained in experiments (3.30 eV in Ref.[32] or 3.75 eV in Ref.[33]).

4.3 Results and discussions

4.3.1 Electronic properties under different strains

It was found from our calculations that, when the compressive strain is above 3%, the electronic properties are very different from those when strain is below 3%. We will thus present the electronic structure in LaO-doped SrTiO$_3$ under zero strain and under $\eta = 3\%$ strain first, and then separately discuss the $\eta = 5\%$ case.

Band structure, electron velocity, and microscopic electron states under $\eta = 0$ or $\eta = 3\%$ strain: Fig.4.3 shows the band structure of LaO-doped SrTiO$_3$ under an $\eta = 3\%$ compressive strain, together with the unstrained case. Obviously one cannot directly compare the absolute orbital energies in two different systems unless they are aligned by, e.g., average potential. Here we are not interested in the absolute orbital energies. Instead we are interested in the *relative* orbital energies with respect to the Fermi energy, since these relative energies can be measured by, e.g., angle resolved photoemission spectroscopy, and are physically meaningful. We therefore set the Fermi energy of individual system as the zero-energy reference, and keep in mind that all orbital energies to be discussed below are relative to the Fermi energy. Furthermore, considering that currently there is a great deal of interest in the conduction states in δ-doped SrTiO$_3$ as a source of electron gas, we also provide in Fig.4.4 a blowup for the conduction bands along the $\Gamma - X$ direction. To obtain useful insight on how individual bands are affected by the inplane strain, we further provide in Fig.4.4 explicit correspondences between the bands in $\eta = 3\%$ and in $\eta = 0$, after analyzing the electron wave functions of individual states at Γ.

For the zero-strain system (see the dotted lines in Fig.4.3 and Fig.4.4), our calculations reveal: (i) The δ-doped SrTiO$_3$ is metallic, which is in sharp contrast with the insulating bulk SrTiO$_3$. The Fermi level of δ-doped SrTiO$_3$ is located at 0.55 eV above the conduction band minimum (CBM). (ii) There are eight conduction bands below E_F in Fig.4.4. Out of these eight bands, seven bands have sharp dispersions along Γ-X. But one band (i.e., band 5 in
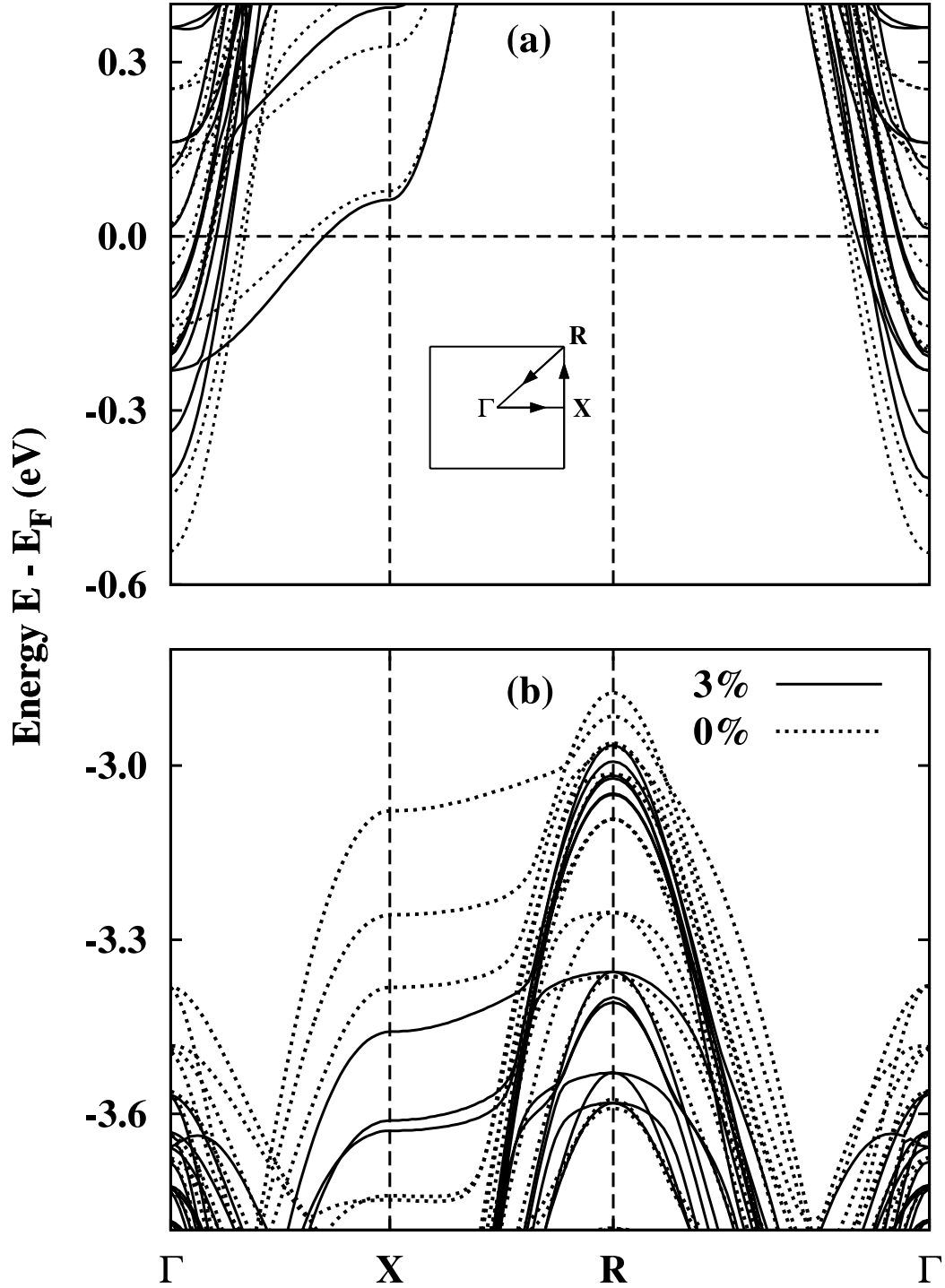
Figure 4.3: Band structures of (a) conduction states and (b) valence states in LaO-doped SrTiO$_3$. Solid lines are for $\eta = 3\%$, while dotted lines are for $\eta = 0$. Inset in (a) shows the 2D Brillouin zone on the xy plane.
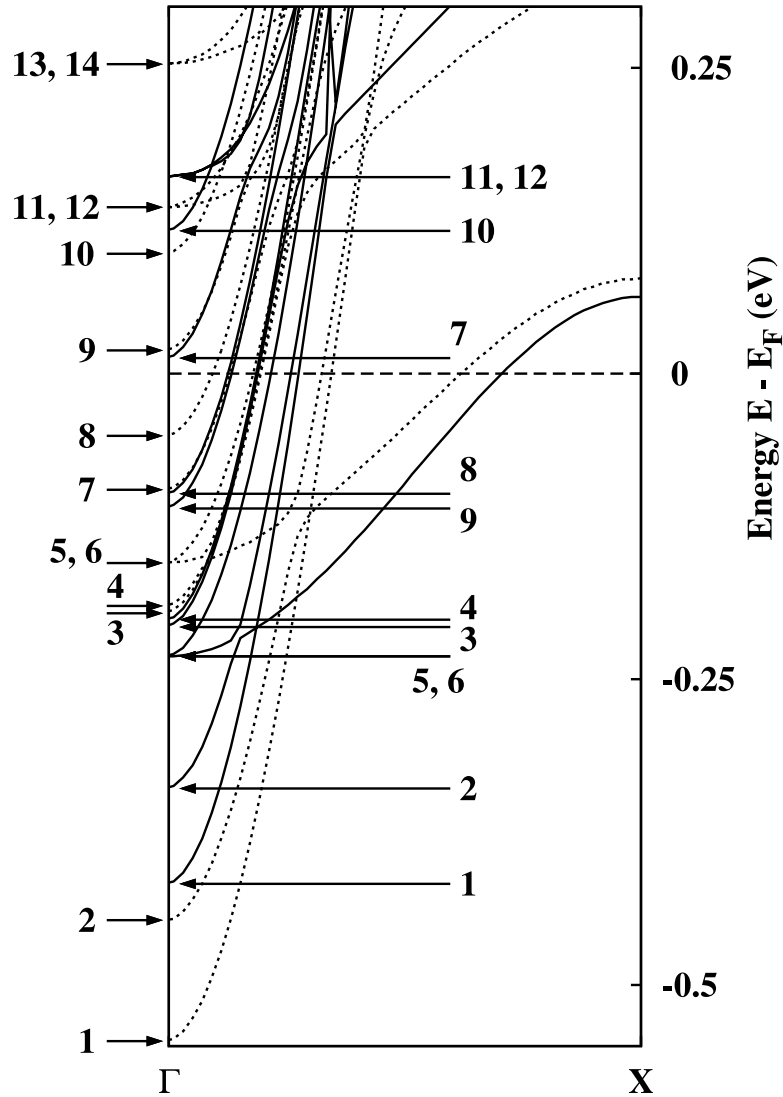
Figure 4.4: A blowup of the conduction band structure along the Γ-X direction. Solid lines are for $\eta = 3\%$ and dotted lines are for $\eta = 0\%$. Bands are labelled by numbers; two bands with the same number indicate the correspondence.

Fig.4.4) is different from the rest of seven bands, by possessing a considerably flat dispersion. When crossing the Fermi level, a sharp band is expected to result in a large electron velocity and high electron mobility. Therefore, seven sharp bands, but not band 5, are expected to display high electron mobility at the Fermi level. (iii) The valence band maximum (VBM) is

located at R in Fig.4.3b, while the CBM is at Γ. The system thus has an indirect band gap. Flat bands also appear in valence states, not along the $\Gamma - X$ direction as the conduction bands, but along the $X - R$ direction.

Our theoretical results on unstrained LaO-doped $SrTiO_3$ are consistent with, and provide some useful understanding for, the experimental observations. In the Hall-resistivity measurement of LaO δ-doped $SrTiO_3$, both high-mobility conducting channel and low-mobility conducting channel were observed along the lateral x direction,[19] which is in agreement with our theoretical finding that both sharp and flat bands exist below E_F in conduction states. It worths pointing out that the existence of flat conduction bands in δ-doped $SrTiO_3$ does not necessarily mean that there is a low-mobility conducting channel since the flat bands may not be located below E_F. Thus it is nontrivial to have both sharp and flat bands below E_F in Fig.4.4. In experiments, large dielectric permeability of $SrTiO_3$ was suggested to be responsible for the high-mobility channel[19]. According to our calculations, the high-mobility channel likely originates from the seven bands with sharp dispersion. Although LaO δ-doped $SrTiO_3$ and the $LaAlO_3/SrTiO_3$ superlattice are two quite different systems, we notice that sharp and flat bands also occur in $(LaAlO_3)_{7.5}/(SrTiO_3)_{7.5}$ superlattice[8].

Upon the impose of a 3% strain, Fig.4.4 shows that the influence of inplane strain on conduction states depends strongly on individual band, namely the effect is band specific. For instance, the lowest two conduction bands (i.e., bands 1 and 2) shift towards E_F after strain. But band 5 (i.e., the flat band) and band 6 (which is degenerate with band 5 at Γ) behave oppositely by shifting away from E_F. And unlike any of the above four bands, bands 3 and 4 are nearly unaffected by the inplane strain. Fig.4.4 also reveals that under a 3% strain there are still eight conduction bands below E_F, although the relative positions and ordering of these bands are different in $\eta = 3\%$ and in $\eta = 0$.

In addition to orbital energies, another key quantity in metallic systems is the size of Fermi wave vector k_F for a given band. This size is experimentally measurable by using the de Haas-van Alphen effect[34, 35]. For a given band index n, k_F depends on the direction

of band dispersion. Here we pay attention to the Γ-X direction, since this is the direction along which electron transport was measured in experiment[19]. Along the Γ-X direction, k_F is determined by the magnitude of wave vector where a given band crosses the Fermi energy in Fig.4.4. For instance, band 5 of the unstrained system in Fig.4.4 crosses E_F at $k_F = 0.32X$. By comparing the k_F wave vectors before and after strain, we see in Fig.4.4 that the compressive strain causes the k_F size to shrink for bands 1 and 2. But for the flat band 5, the strain causes its k_F to expand. These theoretical predictions call for experiments to verify.

We further quantitatively calculate the electron velocity along the x direction according to $v_n(k_F) = \frac{1}{\hbar}\frac{\partial \varepsilon_n(k)}{\partial k}|_{k=k_F}$ for band n and at the wave vector k_F along the Γ-X direction. The result is shown in Table 4.1 for the lowest eight conduction bands. In both $\eta = 0$ and $\eta = 3\%$, the largest electron velocity is found to be from band 1, while the lowest velocity is from band 5. Another key outcome in Table 4.1 is that the velocity of band 1 is 7.6 times of that of band 5, showing a drastic difference.

From the second column in Table 4.1, we see that among the seven sharp bands their velocities also differ, with a clear trend that the velocities tend to decrease from band 1 to band 8. This trend is not accidental, and can be largely explained by the relative energies

Table 4.1: Electron velocities (in units of 10^5m/s) along the x direction for the conduction bands at their respective k_F points. The 2nd column is for $\eta = 0$ and the 3rd column is for $\eta = 3\%$. In the first column, band 9 in parenthesis is for $\eta = 3\%$ since this band moves below E_F after strain.

band n	$v_n(k_F)$ ($\eta = 0$)	$v_n(k_F)$ ($\eta = 3\%$)
1	4.94	4.79
2	4.09	4.06
3	3.44	3.44
4	3.15	3.40
5	0.65	0.73
6	2.97	3.70
7 (9)	2.32	2.80
8	1.96	2.53

of different bands with respect to E_F. Notice that these sharp bands have rather similar curvatures, but are shifted in energy (see the sharp dispersion curves of dotted lines in Fig.4.4). The fact that band 8 has a much higher energy than band 1 indicates that the Fermi energy is closer to the bottom of band 8. Since the bottom of a nearly-parabolic band tends to have a smaller band slope, band 8 thus exhibits a lower electron velocity than band 1 at E_F. By comparing the 3rd column with the 2nd column in Table 4.1, it is evident that the inplane strain affects only slightly the electron velocity for bands 1 and 2, but it alters significantly the velocities for bands 6 and 8 (namely for bands whose bottoms are close to E_F). We notice in Fig.4.4 that the bottoms of bands 6 and 8 move away from E_F after strain, which should increase the velocity according to the similar argument as above. We thus see that how a band shifts with respect to E_F by inplane strain is rather critical, which affects not only the size of Fermi wave vector but also the electron velocity.

To obtain microscopic insight into individual electron states, we next present in Fig.4.5 the electron wave function $|\psi_n(\mathbf{r})|^2$ for the conduction states at Γ in the $\eta = 0$ case. Wave functions for $\eta = 3\%$ are found to be rather similar to those for $\eta = 0$ and are thus not shown. In Fig.4.5, states are marked by numbers, which correspond to the band numbers in Fig.4.4. The location of the LaO layer is indicated by the dotted line in Fig.4.5. As it should be, the conduction states are mainly located at Ti sites and are d-like. Analysis of Fig.4.5 reveals several observations: (i) States 1 and 2 are highly localized near the doping layer, and are thus interface-like. Other states, e.g. states 5 and 7, are far away from the LaO doping layer and are mainly bulk-like. Further, some states, e.g. state 13, are resonant states which have contributions both near the doping layer and in the bulk. The calculations thus predict that the conducting electrons in LaO-doped $SrTiO_3$ are rather interesting—some are 2D-like and some are 3D-like. (ii) Bands 1, 2, 3, 7 and 8 (which are sharp bands) have d_{xy}-like atomic character in Fig.4.5. Note that d_{xy} will look like a p-orbital when projected on a yz plane. On the other hand, flat bands (bands 5, 11 and 13) have d_{yz}-like atomic character. After the different wavefunction characters for band 1 and band 5 are revealed,

68

it is now easy to understand why band 1 is sharp and band 5 is flat along the $\Gamma - X$ direction. Consider two Ti atoms along the x-axis, the interaction between the d_{xy} orbitals of these two neighboring Ti atoms, $dd\pi$, is much stronger than the interaction between the
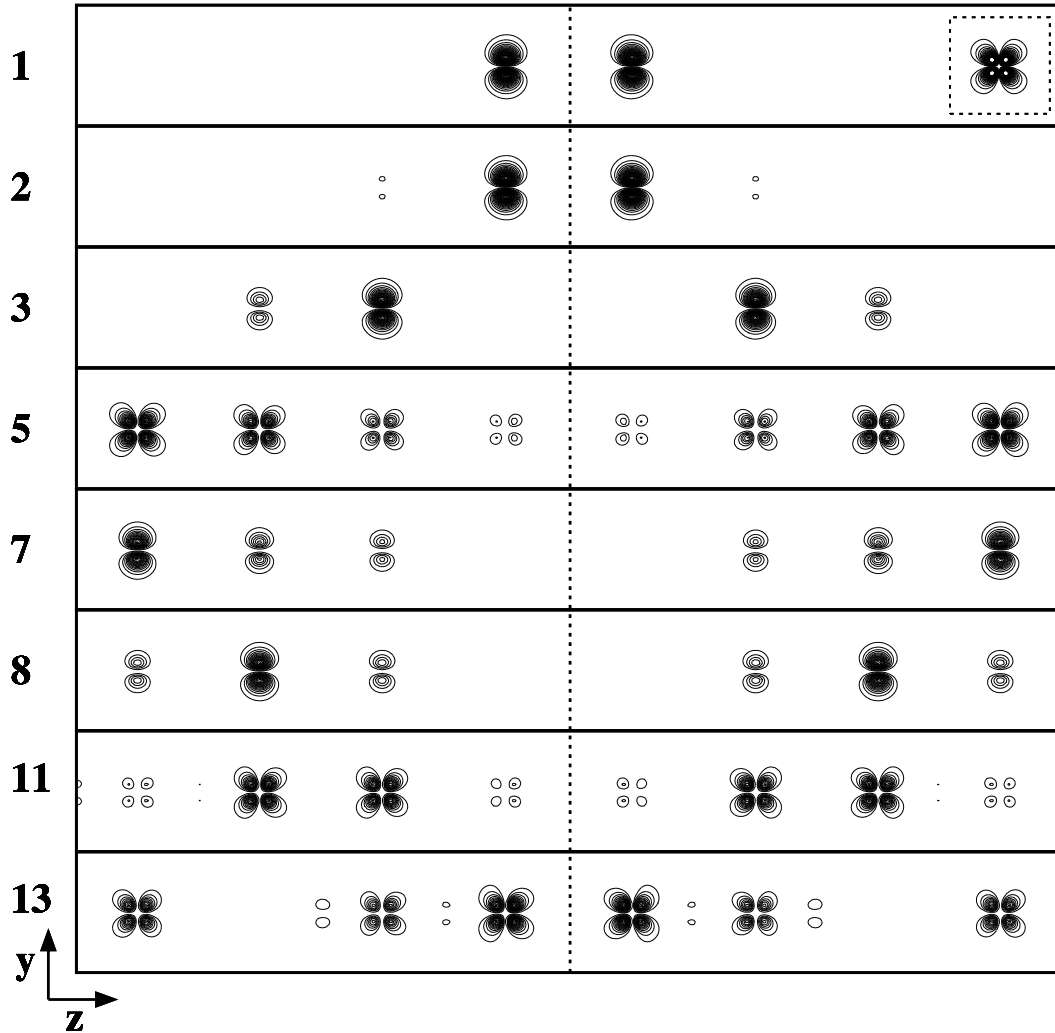
Figure 4.5: Wave functions squared $|\psi_n(\mathbf{r})|^2$ on the yz plane located at $x = 0.6a_0$, for conduction states at Γ in unstrained LaO-doped SrTiO$_3$. Numbers in the left of each panel correspond to the band index in Fig.4.4. We choose the $x = 0.6a_0$ plane rather than the $x = 0.5a_0$ plane, since the latter cuts through the nodes of the d_{xy} orbitals of Ti atoms and leads to zero wavefunction amplitude. The dotted line in the figure denotes the location of the LaO layer. For state 1, the inset gives $|\psi|^2$ on a xy cross-section plane passing a Ti atom, showing that the wavefunction is indeed d_{xy}-like.

d_{yz} orbitals, $dd\delta$, in the tight-binding language[36]. This leads to a sharp dispersion for the former, and a flat dispersion for the latter. (iii) $|\psi(\mathbf{r})|^2$s of states 1 and 2 are very similar, which seemingly violates the orthogonality requirement. The simultaneous occurrence of these two states is puzzling. In fact, these two states are different and can be approximately described as $\psi_1 = \frac{1}{\sqrt{2}}(\phi_l + \phi_r)$ and $\psi_2 = \frac{1}{\sqrt{2}}(\phi_l - \phi_r)$, where ϕ_l and ϕ_r are the wavefunction parts belonging to the left and the right of the doping layer, respectively. Namely, ψ_1 and ψ_2 behave like a bonding and anti-bonding pair. Since ϕ_l and ϕ_r are spatially close, the interaction between them is rather strong when they form the bonding and anti-bonding pair, giving rise to a sizable energy difference between states 1 and 2. Similarly, we find that states 3 and 4 are also a bonding and anti-bonding pair, but with a much smaller splitting in their energies due to the fact that ϕ_l and ϕ_r for these two states are now spatially quite separated. *Band structure and wave functions under $\eta = 5\%$ strain*: Fig.4.6 shows the band structure of LaO-doped SrTiO$_3$ under an $\eta = 5\%$ strain. Several notable differences can be seen between Fig.4.6 and Fig.4.3. First, there are now ten conduction bands below the Fermi level, compared to eight in $\eta = 3\%$. Namely, new bands are now contributing to the conductance. Second, for the conduction states at the zone center Γ, it appears in Fig.4.6a that the lowest ten conduction states form a group (group I), while the other conduction states (which are more than 0.4eV above E_F) form another group (group II). Between two groups is a subband energy difference of $\sim$0.6 eV. Third, in group II, some bands (such as the 11th and 13th bands) show an interesting downward dispersion near the Γ point. These downward dispersions produce negative effective masses for *electrons*. While the effective mass of *hole* is often negative, a negative effective mass for electron is rather unusual. The reason for the downward dispersion is not completely clear. But we notice by analyzing wave functions that these downward bands have significant participation from oxygen orbitals. It is known that the high-energy valence states in SrTiO$_3$ mainly come from oxygen $2p$ orbitals and have downward dispersions. We thus speculate that under sufficient inplane strains, a significant amount of participation from O atoms in the group-II conduction states may

produce the downward dispersion. Regarding the valence bands in Fig.4.6b, we notice that

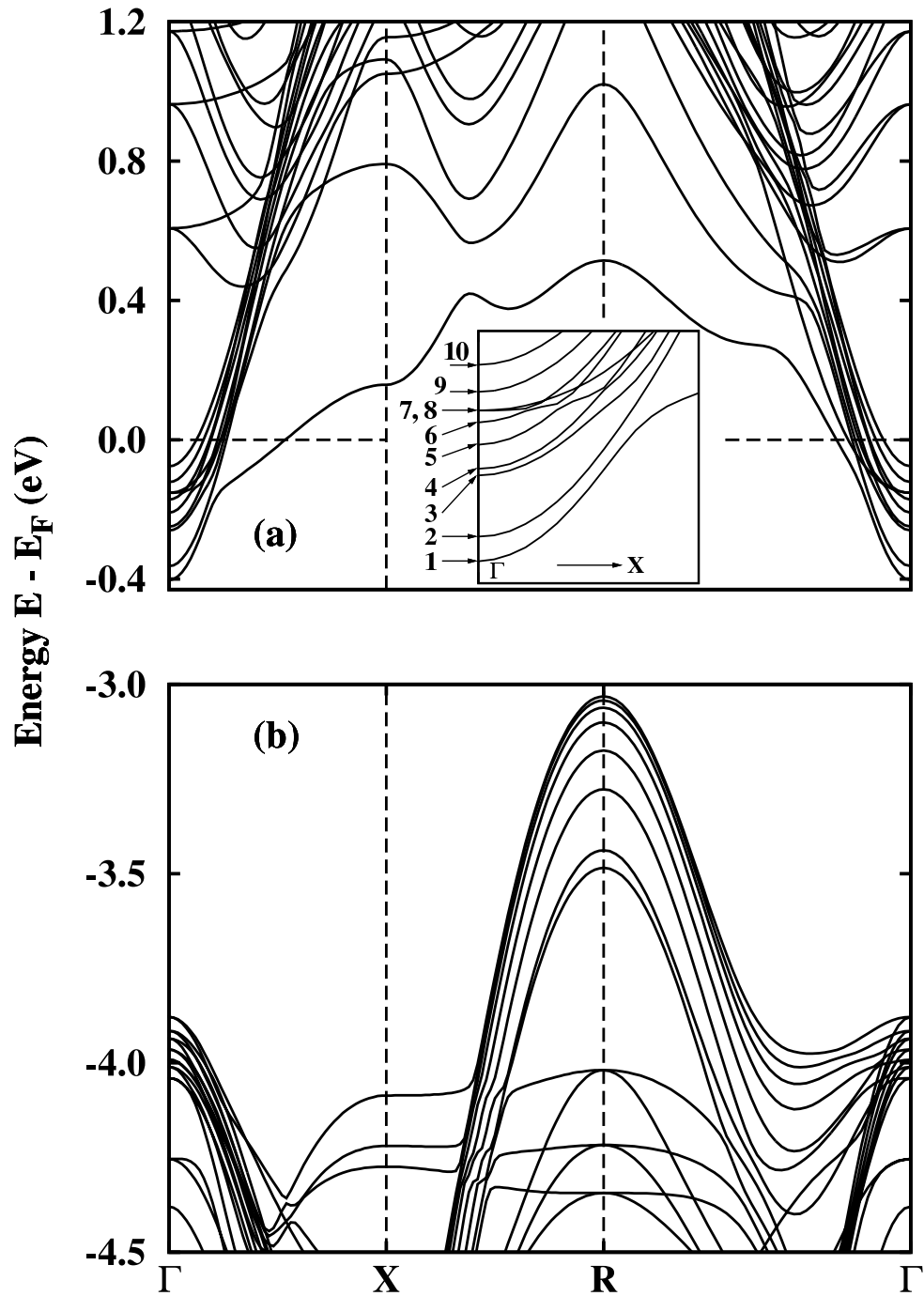
Figure 4.6: (a) Conduction band structure and (b) valence band structure of LaO-doped SrTiO$_3$ under an $\eta = 5\%$ compressive strain. The inset in (a) is a blowup of the conduction band dispersion below E_F along the $\Gamma - X$ direction.

the top eight valence bands at R are all sharp bands, unlike the $\eta = 0$ case in Fig.4.3b where there are a mix of sharp and flat bands.

Fig.4.7 shows the wave functions of the conduction states at Γ for $\eta = 5\%$. A sharp difference occurs between the electron states in Fig.4.7 and those in Fig.4.5, that is, $|\psi(\mathbf{r})|^2$s in Fig.4.5 are symmetric by the mirror-plane of the doping layer, but $|\psi(\mathbf{r})|^2$s in Fig.4.7 are not. Indeed for states such as 1, 2, 5-11 in Fig.4.7, their $|\psi(\mathbf{r})|^2$s are located mainly in one side of the doping layer. This demonstrates the existence of an interesting symmetry breaking on the *microscopic* level. The origin of the symmetry breaking will be investigated in Sec.4.3.1. The result reveals that a inplane strain in δ-doped $SrTiO_3$ can cause drastic changes to microscopic electron states, despite the fact that macroscopically both the $\eta = 3\%$ and $\eta = 5\%$ systems are conducting. Other notable differences also exist. While the flat band (band 5) in Fig.4.5 for $\eta = 0$ is mainly bulk-like, the flat band (band 7) in Fig.4.7 becomes mainly interface-like, with $|\psi(\mathbf{r})|^2$ located near the doping layer. Moreover, we notice for state 11 in Fig.4.7 that there are sizable wavefunction contributions from apical O atoms between two Ti atoms, as well as from base O atoms. As pointed out previously, this O participation may be responsible for the downward dispersion that occurs for band 11.

4.3.2 Structural properties under different strains

To provide the underlying mechanism for the microscopic symmetry breaking of the electron states in the previous section, we now examine the structural properties of the system. Perovskite ABO_3 consists of alternating AO layer and BO_2 layer along the crystalographic [001] direction, i.e., the z-axis direction in this study. The cation-anion displacements (CAD) in each layer, namely $D = z(A) - z(O)$ for the AO layer or $D = z(B) - z(O)$ for the BO_2 layer (where $z(i)$ is the z-axis position of atom i), vanish by symmetry in cubic bulk $SrTiO_3$. In LaO-doped $SrTiO_3$, the cation-anion displacements of individual atomic layers are shown in Fig.4.8, where different curves are for different strains.

Under zero strain (see the empty squares in Fig.4.8), our calculations show that (i) the
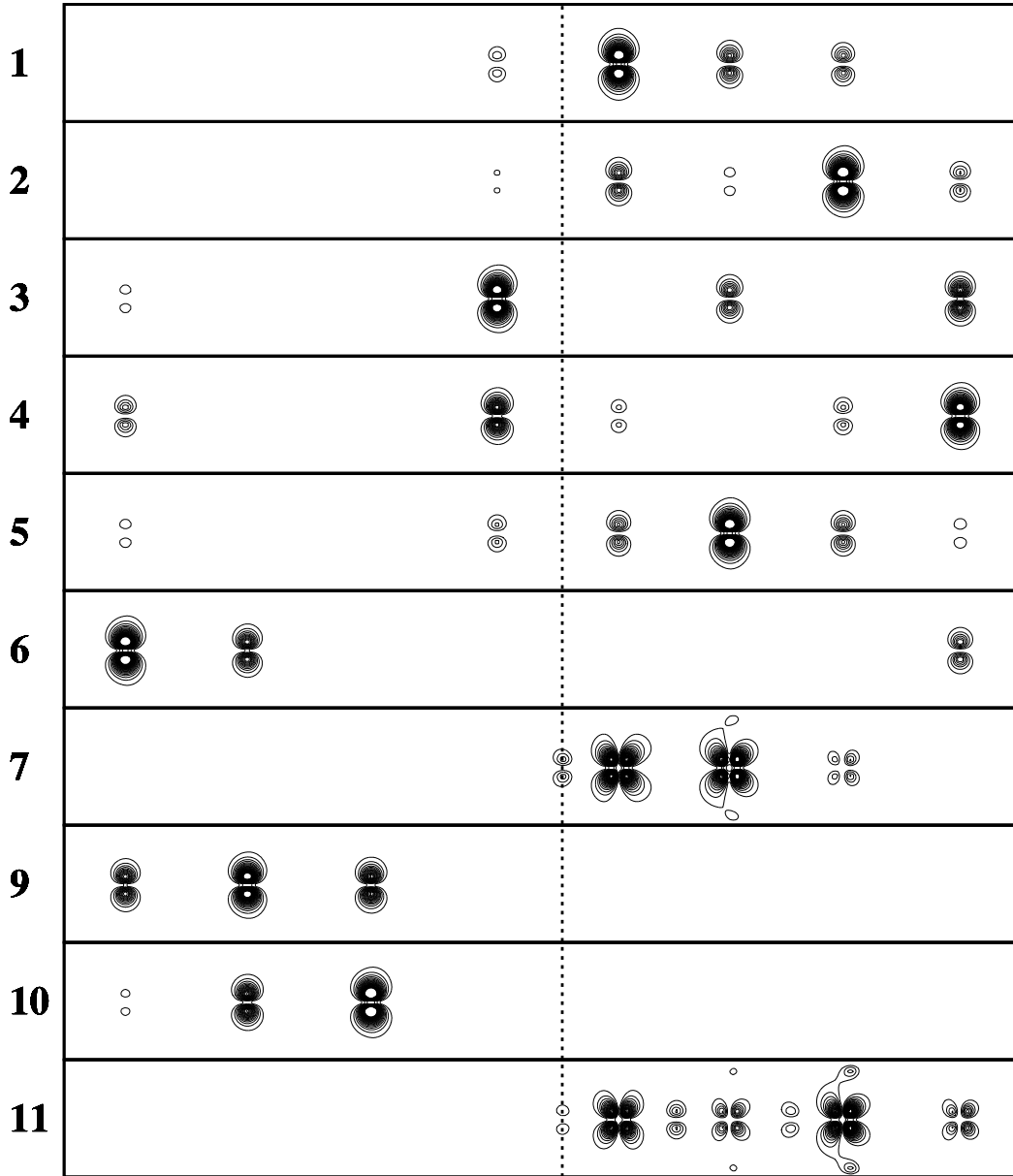
Figure 4.7: Wave functions $|\psi_n(\mathbf{r})|^2$ on the yz plane located at $x = 0.6a$, for the conduction states at Γ in LaO-doped SrTiO$_3$ under $\eta = 5\%$. Numbers in the left of each panel correspond to the band index in the inset of Fig.4.6a.

CAD on the LaO doping layer is null, i.e., La and O are exactly on the same z-plane. (ii) Large CADs are found for those SrO and TiO$_2$ planes that are near the doping layer. The CADs decrease as atomic plane is away from the doping layer. (iii) The CADs under $\eta = 0$ exhibit a mirror-plane symmetry surrounding the LaO layer. For instance, the CADs on the

73

two nearest SrO layers—one to the right and one to the left of the LaO layer—have the same magnitude but opposite sign. These theoretical results can be intuitively explained by the electrostatics of the doping layer. The nominal valences of 3+ in a La ion and 2- in an O ion lead to a net positive *ionic* charge in the LaO doping layer. Note that the total system is charge neutral. The net ionic charge will generate, as schematically shown in Fig.4.1, an electric field **E** which points away from the doping layer. The **E** field is mirror-plane symmetric, and will polarize the SrO and TiO_2 layers such that the cation (anion) in each layer moves away from (close to) LaO, producing positive cation-anion displacements for atomic planes in the right-hand side of the doping layer. When the system subjects to an $\eta = 3\%$ inplane strain, the CADs on SrO and TiO_2 layers in Fig.4.8 show some slight increases in magnitude as compared to the zero-strain case. Nevertheless, the CADs at $\eta = 3\%$ still maintain the mirror symmetry, and the CAD on the LaO layer remains vanishing.

When the inplane η strain increases to 4% or 5%, new phenomena occur in Fig.4.8. First, the CADs no longer have the mirror-plane symmetry. This symmetry breaking can be alternatively seen by noticing in Fig.4.8 that when η increases from 0% to 3%, the CADs to the left of the LaO layer *decrease* while the CADs to the right of the LaO layer *increase*, therefore maintaining the mirror symmetry. However, this is not the case when η increases from 3% to 4%, where the CADs to the left of the LaO layer continue to decrease but the CADs to the right of the LaO layer also decrease. Note that the values of CADs are independent of the choice of coordinate frame. Second, at $\eta = 4\%$ in Fig.4.8, the La and O atoms of the doping layer start to move off-center relative to each other, giving rise to a non-vanishing CAD. Third, the CADs to the left of the LaO layer show an interesting zig-zag pattern at $\eta = 5\%$. This zig-zag pattern is not evident when η is small.

The origin behind the symmetry breaking of CADs at $\eta = 4\%$ and $\eta = 5\%$ is simple and can be attributed to the appearance of strain-induced CADs (or strain-induced ionic polarization). It is known that under a sufficient compressive inplane strain, polarization develops in bulk $SrTiO_3$. Since LaO-doped $SrTiO_3$ is metallic, electrons will screen the
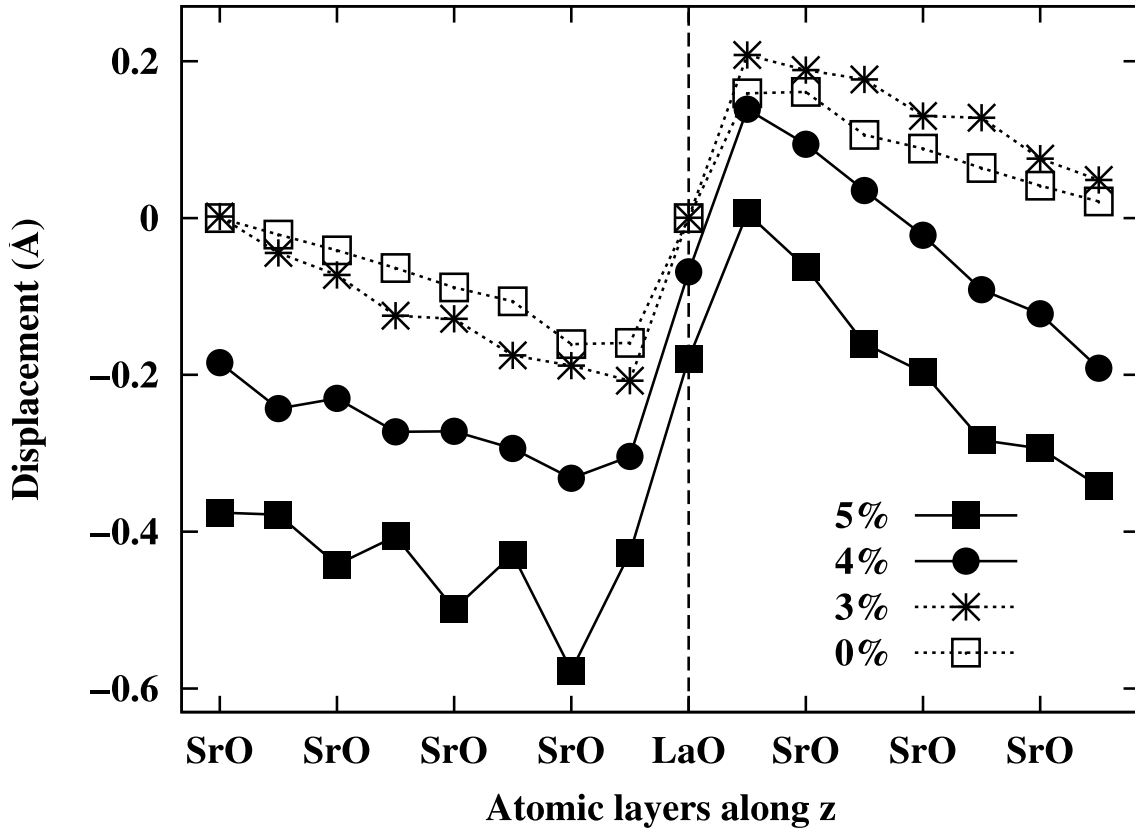
Figure 4.8: Cation-anion displacement of each atomic layer in LaO-doped SrTiO$_3$ under different inplane strains. The AO layers are labeled in the horizontal axis; between two AO layers is a TiO$_2$ layer.

ionic polarization, resulting in a vanishing total polarization. But the ionic polarization, characterized by the cation-anion displacements[37], does not vanish. Therefore, as in bulk SrTiO$_3$, a large inplane strain in LaO-doped SrTiO$_3$ will also trigger off-center displacements of cations with respect to anions. As schematically shown in Fig.4.1, the *field*-induced CAD ($\mathbf{D}_F$) and the *strain*-induced CAD ($\mathbf{D}_S$) have one important difference: the former has a mirror-plane symmetry and the latter does not; $\mathbf{D}_S$'s on different atomic planes point at the same direction. When $\mathbf{D}_S$ occurs, the CADs on different atomic planes shall shift approximately by a similar amount of the same sign, which is indeed confirmed by our numerical results in Fig.4.8 when we compare the $\eta = 3\%$ and $\eta = 4\%$ curves. As a direct
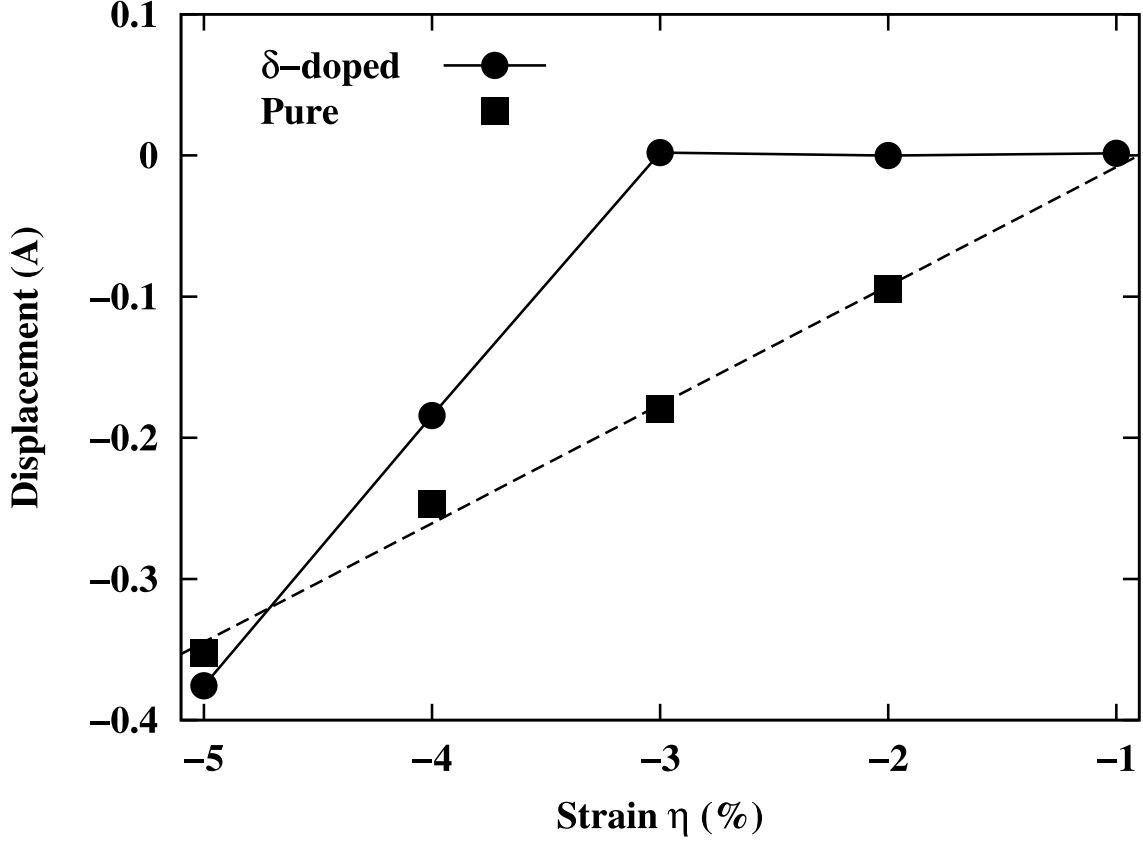
Figure 4.9: Strain-induced cation-anion displacements as a function of strain, in LaO-doped $SrTiO_3$ (dot symbols) and in pure bulk $SrTiO_3$ (square symbols). Extrapolation is used to determine the critical η_c strain.

consequence of the strain-induced $\mathbf{D}_S$, the combined CAD, namely $\mathbf{D}_{tot} = \mathbf{D}_F + \mathbf{D}_S$, does not have a mirror-plane symmetry as shown in Fig.4.1.

It is informative to compare the critical inplane strain η_c (where strain-induced CADs occur), in bulk $SrTiO_3$ and in LaO-doped $SrTiO_3$. The strain-induced CADs in two systems are given in Fig.4.9 as a function of strain. For LaO-doped $SrTiO_3$, the CAD induced by a given strain is determined from Fig.4.8 by using the displacement value on the first SrO layer which is far away from the doping layer and is predominantly bulk-like. For pure bulk $SrTiO_3$, separate calculations are performed to determine the CAD. Fig.4.9 shows that the calculated critical η_c strain is ~1% for bulk $SrTiO_3$, which is close to the value of 0.75%

76

in another calculation[20]. However, in LaO-doped $SrTiO_3$, η_c is found to increase to $\sim3\%$, which is larger than in bulk $SrTiO_3$. One possible reason for this large η_c may be attributed to the existence of depolarization field which is not completely screened in LaO-doped $SrTiO_3$. Nevertheless, 3% is a feasible strain magnitude which can be realized experimentally.

To examine how the cation-anion displacements may affect electronic properties, we depict in Fig.4.10 the planarly averaged macroscopic potential

$$\bar{V}(z) = \frac{1}{L} \int_{z-L/2}^{z+L/2} dz' \frac{1}{a^2} \int V(x', y', z') dx' dy'$$

(where V includes local ionic pseudopotential, Hartree and exchange-correction potentials, and L is chosen to be on the order of a_0). For both $\eta = 0$ and $\eta = 3\%$ cases, we see in Fig.4.10a that $\bar{V}$ has a deep valley at the doping layer, which is consistent with the fact that the doping layer has a net ionic charge and is attractive to electrons. Meanwhile, the deep valley levels off when one moves away from the doping layer, due to electronic and ionic screenings. The potential valley levels off within a distance of $\sim5\text{Å}$, suggesting that the screening length in this system is about 5 Å. Fig.4.10a also reveals that after inplane strain is imposed, the potential near the doping layer increases, but the potential far away from the doping layer (e.g., near $z = 0$) decreases slightly. Combining the wave functions in Fig.4.5 and the potentials in Fig.4.10a also explains why state 1 has the lowest energy among conduction states, since the wave function of this state is localized near the doping layer which is a potential valley.

To explain why wave functions under $\eta = 5\%$ are localized on one side of the doping layer, let us examine the planarly averaged $\bar{V}(z)$ potential in Fig.4.10b. The potential profile at $\eta = 5\%$ differs drastically from those at $\eta = 0$ and $\eta = 3\%$ in Fig.4.10a in terms of that (i) the average potential in Fig.4.10b is asymmetric and (ii) a pronounced potential discontinuity occurs in Fig.4.10b at $z \approx 13\text{Å}$ near the doping LaO layer. The magnitude of discontinuity is ~1.5 eV. It is known that potential discontinuity is often caused by a dipole layer. In
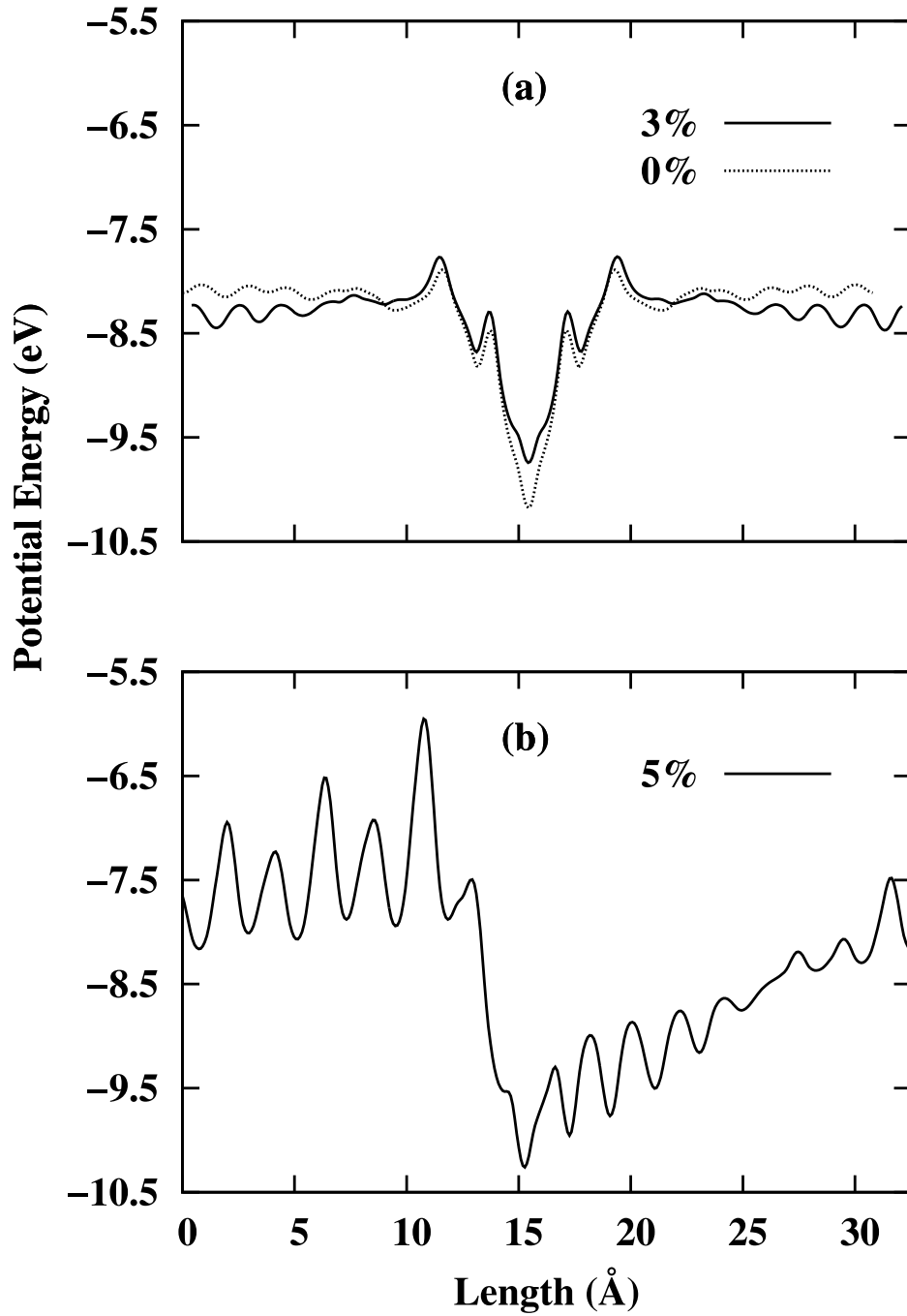
Figure 4.10: Macroscopically averaged potential $\bar{V}(z)$ as a function of z for (a) $\eta = 0$ and $\eta = 3\%$, and (b) $\eta = 5\%$. In (a), the mirror plane (i.e., the LaO layer) is placed at the center, and the average potential is aligned.

the considered system, two sources may contribute to the formation of the dipole layer: one is the *ionic* relative displacement between La and O, and the other is the *electronic* charge accumulation at the interface. To examine which contribution is important, we constrain La and O to be in the same plane (thus eliminating the ionic contribution), and we find that the potential discontinuity still exists with similar magnitude. The electron charge accumulation at the interface is thus the main reason responsible for producing the dipole layer and the potential discontinuity. LaO-doped $SrTiO_3$ is metallic, and the mobile electrons accumulate in the nearby of the doping layer to screen the strain-induced ionic polarization. To further verify this conclusion, we replace the LaO layer by a SrO layer and calculate the potential in eight-cell pure $SrTiO_3$ under the 5% inplane strain. We find that the potential discontinuity disappears, confirming that the electron charge accumulation is caused by δ-doping. The asymmetric potential causes the wave functions at $\eta = 5\%$ to be also asymmetric, which can be viewed as a microscopic manifestation of the mirror-plane symmetry breaking.

4.4 Summary

First-principles density functional calculations were performed to study the biaxial-strain effects in LaO-doped $SrTiO_3$. Both structural and electronic properties are examined. The theoretical results obtained here on structural properties may be verified using x-ray diffraction, while the results on the electronic properties could be tested using angle-resolved photoemission spectroscopy or the de Haas-van Alphen effect. Our specific findings are summarized below.

When strain is below 3%, calculations reveal the following electronic properties. (i) Seven conduction bands of sharp dispersions and one conduction band of flat dispersion are below E_F along the $\Gamma - X$ direction. High-mobility electrons and low-mobility electrons thus both contribute to the conductivity along the x direction, which is consistent with the experimental observation. (ii) At the Fermi level along the $\Gamma - X$ direction, the electron velocity of (sharp) band 1 is about 7.6 times of (flat) band 5. The electron velocities of different sharp bands also vary significantly, and correlate well with their relative energies with respect to E_F. Inplane strain is found to change significantly the electron velocity for bands whose bottoms are near E_F, for instance, bands 6 and 8 in Table 4.1. (iii) For sharp bands 1 and 2, the inplane strain causes their energies to shift toward E_F and the sizes of their Fermi wave vectors to shrink along the $\Gamma - X$ direction. The opposite is true for flat band 5. (iv) Microscopic insights are provided for the low-energy conduction states. Along the $\Gamma - X$ direction, sharp bands are Ti d_{xy}- or d_{xz}-like, while flat bands are Ti d_{yz}-like. Furthermore, different electron states are found to be localized in different spatial regions along the z-direction. Some conducting electrons are 2D-like, and some are 3D-like. In other words, 2D and 3D conducting electrons coexist in LaO-doped $SrTiO_3$, which may allow to examine electron behaviors of different dimensions. (v) The electron potential shows a deep valley at the LaO layer, and the valley levels off within $\sim$5 Å.

When $\eta > 3\%$, (vi) ten conduction bands are below E_F that contribute to the conductivity along the x direction. Out of these ten bands, once again only one band is flat. (vii)

Several conduction bands in group II show downward dispersions near Γ, producing negative effective masses for electrons. (viii) The wave functions of the conduction states are altered drastically, owing to the emergence of strain-induced ionic polarization. (ix) The electron potential shows a pronounced discontinuity. The discontinuity originates from the electron accumulation near the doping layer.

Regarding the structural properties, we reveal (x) when η is small and below 3%, only field-induced CADs exist and are caused by the ionic charge of the LaO layer. The field-induced CADs display a mirror-plane symmetry, and the CAD on the doping layer is null. (xi) When η is increased above 3%, strain-induced CADs start to occur on SrO and TiO_2 layers, and meanwhile the LaO doping layer also shows a nonzero cation-anion displacement. The occurrence of strain-induced CADs leads to the symmetry breaking of the mirror reflection. (xii) The critical η_c strain in LaO-doped $SrTiO_3$ ($\eta_c = 3\%$) differs significantly from the value in pure $SrTiO_3$ ($\eta_c = 1\%$) due to an incomplete screening of the depolarization field.

This chapter has been submitted for publication in:

Structural and electronic properties of LaO δ-doped $SrTiO_3$ caused by biaxial strain, Rajendra Adhikari and Huaxiang Fu, Phys. Rev. B.

Bibliography

[1] J. Heber, Nature (London) **459**, 28 (2009).

[2] H.Y. Hwang, Y. Iwasa, M. Kawasaki, B. Keimer, N. Nagaosa, and Y. Tokura, Nat. Mater. **11**, 103 (2012).

[3] A. Ohtomo and H. Y. Hwang, Nature (London) **427**, 423 (2004).

[4] A. Brinkman, M. Huijben, M. van Zalk, J. Huijben, U. Zeitler, J. C. Maan, W. G. van der Wiel, G. Rijnders, D.H.A. Blank, and H. Hilgenkamp, Nat. Mater. **6**, 493 (2007).

[5] N. Reyren, S. Thiel, A.D. Caviglia, L.F. Kourkoutis, G. Hammerl, C. Richter, C.W. Schneider, T. Kopp, A.-S. Retschi, D. Jaccard, M. Gabay, D. A. Muller, J.-M. Triscone, J. Mannhart, Science **317**, 1196 (2007).

[6] R. Pentcheva and W.E. Pickett, Phys. Rev. Lett. **99**, 016802 (2007).

[7] S. Okamoto, A.J. Millis, and N.A. Spaldin, Phys. Rev. Lett. **97**, 056802 (2006).

[8] Z. Popovic, S. Satpathy, and R.M. Martin, Phys. Rev. Lett. **101**, 256801 (2008).

[9] J. Lee and A.A. Demkov, Phys. Rev. B **78**, 193104 (2008).

[10] D.R. Hamann, D.A. Muller, and H. Y. Hwang, Phys. Rev. B **73**, 195403 (2006).

[11] P. Larson, Z.S. Popovic, and S. Satpathy, Phys. Rev. B **77**, 245122 (2008).

[12] K. Janicka, J.P. Velev, and E.Y. Tsymbal, Phys. Rev. Lett. **102**, 106803 (2009).

[13] M. Stengel and D. Vanderbilt, Phys. Rev. B **80**, 241103 (2009).

[14] L. Zhang, X.-F. Zhou, H.-T. Wang, J.-J. Xu, J. Li, E.G. Wang, and S.-H. Wei, Phys. Rev. B **82**, 125412 (2010).

[15] S. Thiel, G. Hammerl, A. Schmehl, C. W. Schneider, and J. Mannhart, Science **313**, 1942 (2006).

[16] C. Cen, S. Thiel, J. Mannhart, and J. Levy, Science **323**,1026 (2009).

[17] A. F. Santander-Syro, O. Copie, T. Kondo, F. Fortuna, S. Pailhes, R. Weht, X.G. Qiu, F. Bertran, A. Nicolaou, A. Taleb-Ibrahimi, P. Le Fevre, G. Herranz, M. Bibes, N. Reyren, Y. Apertet, P. Lecoeur, A. Barthelemy, and M. J. Rozenberg, Nature (London) **469**, 189 (2011).

[18] A. Ohtomo, D.A. Muller, J.L. Grazul, and H.Y. Hwang, Nature (London) **419**, 378 (2002).

[19] J.S. Kim, S.S.A. Seo, M.F. Chisholm, R.K. Kremer, H.-U. Habermeier, B. Keimer, and H.N. Lee, Phys. Rev. B **82**, 201407 (2010).

[20] A. Antons, J.B. Neaton, K.M. Rabe, and D. Vanderbilt, Phys. Rev. B **71**, 024102 (2005).

[21] Y. Yao and H. Fu, Phys. Rev. B **80**, 035126 (2009).

[22] P. Giannozzi, S. Baroni, N. Bonini, M. Calandra, R. Car, C. Cavazzoni, D. Ceresoli, G.L. Chiarotti, M. Cococcioni, I. Dabo, A. Dal Corso, S. Fabris, G. Fratesi, S. de Gironcoli, R. Gebauer, U. Gerstmann, C. Gougoussis, A. Kokalj, M. Lazzeri, L. Martin-Samos, N. Marzari, F. Mauri, R. Mazzarello, S. Paolini, A. Pasquarello, L. Paulatto, C. Sbraccia, S. Scandolo, G. Sclauzero, A. P. Seitsonen, A. Smogunov, P. Umari, R. M. Wentzcovitch, J. Phys. C **21**, 395502 (2009).

[23] P. Giannozzi *et al.*, http://www.quantum-espresso.org.

[24] N. Troullier and J. L. Martins, Phys. Rev. B **43**, 1993 (1991).

[25] I.I. Naumov and H. Fu, Phys. Rev. B **72**, 012304 (2005); Y. Yao and H. Fu, Phys. Rev. B **82**, 174119 (2010).

[26] A. A. Knizhnik, I. M. Iskandarova, A. A. Bagatur'yants, B. V. Potapkin, L.R.C. Fonseca, and A. Korkin, Phys. Rev. B **72**, 235329 (2005).

[27] J. H. Haeni, *et al.*, Nature (London) **430**, 758 (2004); F. He, B. O. Wells, and S. M. Shapiro, Phys. Rev. Lett. **94**, 176101 (2005).

[28] S. Lany and A. Zunger, Phys. Rev. Lett. **98**, 045501 (2007).

[29] A. Janotti and C. G. Van de Walle, Nat. Mater. **6**, 44 (2007).

[30] T.R. Paudel and W. R. L. Lambrecht, Phys. Rev. B **77**, 205202 (2008).

[31] S.-G. Lim, S. Kriventsov, T. N. Jackson, J. H. Haeni, D. G. Schlom, A. M. Balbashov, R. Uecker, P. Reiche, J. L. Freeouf, and G. Lucovsky, J. Appl. Phys. **91**, 4500 (2002).

[32] Y. Tezuka, S. Shin, T. Ishii, T. Ejima, S. Suzuki, and S. Sato, J. Phys. Soc. Jpn. **63**, 347 (1994).

[33] K. van Benthem, C. Elsasser, and R. H. French, J. Appl. Phys. **90**, 6156 (2001).

[34] N.W. Ashcroft and N.D. Mermin, *Solid State Physics*, (Thomson Learning, 1976), chapter 14.

[35] L. Landau, Z. Phys. **64**, 629 (1930); D. Shoenberg, Proc. Roy. Soc. A **170**, 341 (1939).

[36] J.C. Slater and G.F. Koster, Phys. Rev. **94**, 1498 (1954).

[37] X. Wu, O. Dieguez, K.M. Rabe, and D. Vanderbilt, Phys. Rev. Lett. **97**, 107602 (2006).

Conclusion

The conclusions of this Dissertation are summarized below.

1) Conclusion from Ferroelectric $Pb(Zr_{0.5}Ti_0.5)O_3$ (PZT) nanotube array.
Finite-temperature first-principles-based simulations are used to determine the structural and polarization properties of ferroelectric $Pb(Zr_{0.5}Ti_{0.5})O_3$ (PZT) nanotube array embedded in matrix medium of different ferroelectric strengths. Various interesting properties are found, including (i) that the system can behave either 3D-like, or 2D-like, or 1D-like; and (ii) the existence of an unusual structural phase in which a 180-degree stripe domain coexists with vortex. Furthermore, we show in a PZT tube array that a vortex phase can *spontaneously* transform into a ferroelectric phase of polarization by temperature alone, without applying external electric fields. Microscopic insights for understanding these properties are provided.

2) Conclusion from LaO δ-doped $SrTiO_3$.
Cation-anion displacements (CAD) and electronic properties caused by compressive biaxial inplane strains in LaO δ-doped $SrTiO_3$ are studied by first-principles density functional calculations. When strain is small and below 3%, we find (i) only field-induced CADs exist, which leads to symmetric electron states surrounding the doping layer; (ii) Seven conduction bands with sharp dispersions and one conduction band with flat dispersion are below the Fermi energy along the $\Gamma - X$ direction, revealing that both high-velocity and low-velocity electrons contribute to the conductivity along the x direction; (iii) Inplane strain causes the size of Fermi wave vector to shrink for the lowest two sharp bands along $\Gamma - X$. But it causes an opposite effect on the flat band. (iv) In LaO-doped $SrTiO_3$, some electrons are 2D-like, and some are 3D-like, which coexist in the same system. On the other hand, when strain is increased above a critical value of 3%, the system shows drastically different structural

84

and electronic behaviors. More specifically, (v) several conduction bands display unusual downward dispersions, producing negative effective masses for electrons; (vi) A symmetry breaking occurs to microscopic electron states, and the symmetry breaking originates from the strain-induced CADs; (vii) The electron potential shows a pronounced discontinuity near the doping layer. The study reveals that biaxial inplane strain can effectively modify the electronic properties in δ-doped $SrTiO_3$ for the purpose of oxide electronics.

Appendix

Publications

<u>Rajendra Adhikari</u> and H. Fu, *Structural and electronic properties of LaO δ-doped SrTiO₃ caused by biaxial strain*, Phys. Rev. B (submitted).

<u>Rajendra Adhikari</u> and H. Fu, *Interesting properties of ferroelectric Pb(Zr_{0.5}Ti_{0.5})O_3 nanotube array embedded in matrix medium*, Journal of Applied Physics (accepted).

<u>R. Adhikari</u>, Y. Cheng, and A. E. Meyerovich, *Quantum size effect and biased diffusion of gravitationally bound neutrons in a rough waveguide,*
Phys. Rev. A **75**, 063613 (2007).

Presentations

Jan 29- Feb 1, 2012 Argonne, Illinois: Fundamental Physics of Ferroelectrics and Related Materials.
Poster, <u>Rajendra Adhikari</u> and H. Fu, *Electronic structure of LaO doped SrTiO₃.*

March 21-25, 2011 Dallas, Texas: APS March Meeting 2011.
Oral, <u>Rajendra Adhikari</u> and H. Fu, *Ferroelectric polarization of Pb(Zr_{0.5}Ti_{0.5})O_3 nanotube array.*

Jan 31- Feb 5, 2010 Aspen, Colorado: Advances in the Fundamental Physics of Ferroelectrics and related materials.
Poster, <u>Rajendra Adhikari</u> and H. Fu, *Ferroelectric properties of modulated PZT nanowires.*